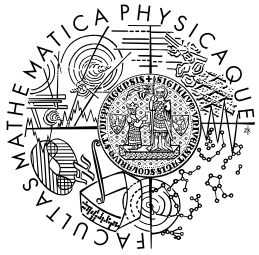

FACULTY
OF MATHEMATICS
AND PHYSICS
Charles University

BACHELOR THESIS

Barbora Křivská

Transmission Electron Microscopy of Al-Mg Aluminum Alloys with Addition of Sc and Zr

Department of Physics of Materials

Supervisor of the bachelor thesis:	RNDr. Michaela Šlapáková, Ph.D.
Study programme:	Physics
Study branch:	General physics

Prague 2019

I declare that I carried out this bachelor thesis independently, and only with the cited sources, literature and other professional sources.

I understand that my work relates to the rights and obligations under the Act No. 121/2000 Sb., the Copyright Act, as amended, in particular the fact that the Charles University has the right to conclude a license agreement on the use of this work as a school work pursuant to Section 60 subsection 1 of the Copyright Act.

In Prague date ..... signature of the author

I would like to acknowledge everyone who helped me during my studies. First and foremost, I would like to express my appreciation above all to my supervisor RNDr. Michaela Šlapáková, Ph.D. for getting initial training in electron microscopy, giving advice and help during writing my bachelor thesis. I would also to thank to doc. RNDr. Miroslav Cieslar, CSc. for consultations and a great patience with me. My thanks also belong to RNDr. Jitka Stráská, Ph.D. for EBSD measurements, Ing. Jana Kálalová and Marta Čepová for acquainting me with the laboratory and light optical microscopy. Last but not least, I would like to thank to my family for their love and support. Special thanks go to Martin Kihoulou for (not only) LaTeX advice, without whom it would be impossible to arrange all my micrographs in my thesis to a desired order.

Title: Transmission Electron Microscopy of Al-Mg Aluminum Alloys with Addition of Sc and Zr

Author: Barbora Křivská

Department: Department of Physics of Materials

Supervisor: RNDr. Michaela Šlapáková, Ph.D., Department of Physics of Materials

Abstract: The microstructure and its evolution during isochronal annealing of a twin roll cast Al–3.2Mg–0.19Sc–0.14Zr (wt.%) alloy was investigated by light optical microscopy and electron microscopy. Two procedures – equal channel angular pressing and annealing at 300 °C for 8 h were applied to enhance mechanical properties of the alloy. The annealing led to the precipitation of a fine dispersion of Al_3(Sc,Zr) particles providing an increase of ∼20 HV in the Vickers microhardness. Equal channel angular pressing refined significantly the microstructure and raised the microhardness by about 30 HV. Applying of the 300 °C / 8 h both before and after equal channel angular pressing did not induce further strengthening. However, the precipitation of the Al_3(Sc,Zr) phase had a stabilizing effect when the material was exposed to the subsequent isochronal annealing.

Keywords: Al–Mg–Sc–Zr alloy, Twin-roll casting, Equal channel angular pressing, Microstructure, Hardness.

Contents

Introduction

Aluminum is a very perspective metal with an application potential in several branches of an industry due to its exceptional properties such as low density, corrosion resistance caused by a formation of a thin layer of Al_2O_3 on the surface, good ductility, electrical conductivity etc. It is used for cans and kitchen utensils production, or it can replace copper in electrical power lines, because aluminum is cheaper and has three-times lower density than copper [1, 2].

The main disadvantage of a pure aluminum is its low strength. Fortunately, there are several procedures, how to suppress this feature and increase the use value of aluminum. The most common procedures are the following ones. Firstly, increase of inherent defects density, such as dislocations, grain boundaries and subgrain boundaries. However, this type of defects does not persist at higher temperatures. Another possibility is an addition of alloying elements which could harden the material due to the formation of stress fields that make dislocation motion more difficult. Alloying elements can also effectively pin boundaries and dislocations and preserve them to higher temperatures. One of those elements is magnesium, a very light metal, that strongly strengthens aluminum without any formation of strengthening phases and shifts dislocation recovery and recrystallization to higher temperatures. With other alloying elements, e.g. Cu or Si, magnesium forms some metastable phases that are responsible further hardening of the alloy [3]. These Al-Mg based alloys are nowadays widely used in aircraft, aerospace and automotive industries [4, 5]. Especially sheets and strips are cast for production of skins of aircraft, cockpits, fuel tanks, heat shields etc. An additional stabilizing of the microstructure can be achieved by alloying of the material by Sc and Zr and by a subsequent precipitation of Sc and Zr containing particles [6].

However, conventionally cast Al-Mg alloys suffer from a detrimental property - formation of Al_3Mg_2 phase segregating along a special type of grain or subgrain boundaries. If these boundaries are parallel to the metal surface and chlorine ions appear in their vicinity, the galvanic corrosion emerge on the strip surface. Moreover, due to a lamelar structure with flat grains formed after hot rolling (a necessary procedure after a conventional direct chill casting), Al_3Mg_2 phase forms continuous layers and the corrosion can easily proceed following these layers along the grain boundaries. As a result, a thin layers from the strip can be released from the material like sheets from a book [7, 8].

Recrystallization is the most common method used for the elimination of flat grains. However, the recrystallization temperature is generaly very high and results in Al_3(Sc,Zr) particles overaging in Sc and Zr containing alloys and in a loss of the precipitation hardening effect. Therefore, another method resulting in a suppression of the layered structure is intensively searched.

A promising alternative technique might be a continuous casting (twin-roll casting, twin-belt casting) of the metal sheet to the final thickness and use of some of severe plastic deformation methods for a grain refinement. The aim of this work is to find out how a twin roll cast Al-Mg-Sc-Zr strip subjected to the equal channel angular pressing behaves at elevated temperatures.

1. Overview of studied topics

1.1 Aluminum

Aluminum is lightweight, silvery-white metal of a boron group with the atomic number 13. It is the most common metal in the Earth's crust and the third most frequent element after oxygen and silicon [9, 10]. However, due to its chemical reactivity, it does not appear as a pure metal but as a compound in many different minerals. The principal aluminum ore is bauxite, which consists of several aluminum oxides and hydroxides combined with iron oxides. The first product of bauxite is alumina, the aluminum oxide Al_2O_3, from which is the pure aluminum produced by electrolysis [11, 12]. Basic characteristics of aluminum are summarized in Tab. 1.1.

Table 1.1: Basic atomic and physical properties of aluminum

Element Properties	
atomic number	13
atomic weight	26.9815
melting point	660 °C
boiling point	2 467 °C
density	2.70 g.cm^{-3} (at 20 °C)
valence	3
electron configuration	$1s^2\ 2s^2\ 2p^6\ 3s^2\ 3p^1$

Aluminum crystallizes in a face-centered cubic (FCC) structure with the lattice parameter $a = 4.046$ Å [13]. Commercially pure as-cast aluminum contains (besides some impurities) a low density of isolated dislocations. Number of dislocations increases during mechanical treatment. Dislocations form tangles leading to a material strengthening. If alloying elements are present in the solid solution during the deformation, the dislocation mobility is reduced by an interaction with solute atoms. A more rapid buildup of dislocations is then responsible for a more rapid work hardening. However, the strengthening effect induced by dislocations could be lost during the exposition of the material to higher temperatures [14].

1.2 Alloying of aluminum

Nowadays, metals are usually alloyed with various elements enhancing their mechanical properties, corrosion resistance, etc. Alloying elements can essentially strengthen the material because they cause a formation of stress field and pin the dislocations. There are two types of strengthening induced by foreign atoms: solid solution hardening – alloying atoms are dispersed in the solid solution, or precipitation hardening – alloying elements are aggregated together with matrix

atoms and form coherent or incoherent precipitates, which also represent obstacles for the dislocation motion.

As a point defect, the solute atom interacts with other lattice defects. Especially dislocations motion is hindered and solutes contribute to the strengthening. Stress σ required for the dislocation motion is described by Peach-Koehler equation (Peach and Koehler gave an equation for the force on a line element of the dislocation in a stress field [15])

$$\sigma = \frac{F_m}{bL}, \tag{1.1}$$

where F_m is a force imposed by obstacles on the dislocation, L is the distance between obstacles along the dislocation line and b is a dislocation Burgers vector.

The level of the impurity concentration gives different predictions. A low concentration leads to a Fleischer model [16] of single pinning points. The strength scales with the solute concentration c in this given case as

$$\sigma \approx c^{1/2}. \tag{1.2}$$

The Labush theory holds true for higher concentrations [17]. It assumes a continuous density of pinning centers along the dislocation line. The relation between stress and the solute concentration is

$$\sigma \approx c^{2/3}. \tag{1.3}$$

A precipitation hardening is another effect generated by alloying elements. Coherent particles can be passed by dislocations. Dislocations cut the particle on the same slip plane as in the matrix but much higher stress is required in comparison with the motion through the matrix. There are several mechanisms that contribute to the strengthening – antiphase boundary formation, increase of the interfaces after shearing, coherency strain hardening, different stacking fault energy etc. If we consider the Labusch theory and assume a spherical shape of the particle, the relation for each contribution of the coherent precipitation hardening is given

$$\sigma \approx f^{\frac{2}{3}} r_0^{\frac{1}{3}} F^{\frac{4}{3}}, \tag{1.4}$$

where f is the volume fraction of the precipitates, r_0 radius of the particles and F is the interaction force characteristic for the given type of contribution [18].

Incoherent precipitates behave as strong impenetrable obstacles, so dislocations bow out between them. Particles are then bypassed by the dislocation by a mechanism, which creates a separate dislocation loop and leaves it behind or around the particle. This mechanism is called after E. Orowan and it can be described by modified Orowan-Ashby equation

$$\sigma = \frac{Gb}{A(L-D)} \ln\left(\frac{D}{2b}\right), \tag{1.5}$$

where G is the shear modulus, L the distance between the particles, D their diameter and A is 2π for a screw dislocation and $2\pi(1-\nu)$ for an edge dislocation, ν is the Poisson's ratio [19].

1.2.1 Magnesium

Magnesium belongs to a group of elements responsible for the solid solution strengthening of aluminum. Main applications of Al-Mg alloys are in the aerospace and automotive industries due to their excellent corrosion resistance, high strength and a good weldability when compared to any other Al alloys [4, 5].

When magnesium content exceeds 3.5 wt.%, highly anodic phase Al_3Mg_2 may precipitate within grains or preferentially on grain boundaries [20], resulting from thermal operations at slightly elevated temperatures (100 °C). A continuous precipitation along grain boundaries causes undesirable corrosion propagation and degradation of the material [21]. As a result, rolled Al-Mg-based materials widely used for the fabrication of airplane skins are susceptible to exfoliation corrosion, because they are exposed to an elevated temperature during the service and the corrosion propagates fast due to elongated and flat grain structure induced by the rolling process.

Requirement to find an effective method of Al-Mg sheets production and treatment preserving the advantages of this alloy and suppressing the seamy side, are a subject of intensive studies nowadays.

1.2.2 Mg + Mn and small Si addition

Composition within this system forms important classes of non-heat-treatable alloys. Technical labeling of the commercial Al-Mg-Mn alloys is 5XXX or 6XXX with the addition of Si. Manganese added to Al-Mg alloy increases the hardness, but decreases the ductility. Increasing amounts of either magnesium or manganese intensify the difficulty of a fabrication and increase the tendency toward cracking during hot rolling. The two main advantages of manganese addition are that the precipitation of the magnesium phase is more homogeneous throughout the structure, and that for a given increase in strength, manganese allows a lower magnesium content and ensure a greater degree of stability of the alloy. An addition of Si strengthen Al-Mg-Mn alloy by a precipitation of metastable phases during heat treatments at moderate temperatures (100 – 200 °C) [22]. Phases, that can be found in the as-cast alloy, are e.g. non-equilibrium Mg_2Si, $MnAl_6$ or $\alpha - AlMnSi$ [23].

1.2.3 Scandium and zirconium

Zirconium in a minor addition to Al-Mg alloys may reduce stress corrosion susceptibility. It also imparts a grain refining effect. Zirconium additions in the range 0.1 to 0.3 wt.% are used to form a fine precipitate of intermetallic particles that inhibit recovery and recrystallization. An increasing number of alloys use zirconium additions to increase the recrystallization temperature and to control the grain structure. Higher levels of zirconium are employed in some superplastic alloys to retain the required fine substructure during elevated-temperature forming. After a heat treatment the presence of metastable Al_3Zr coherent dispersoids with average size 5 – 10 nm is required in order to reach a maximal strength.

Moreover, if scandium is added to Al-Zr, further stabilization of the microstructure can be achieved. The maximal hardening effect was observed between 350 °C and 450 °C in binary Al-Zr alloys [24]. Binary Al-Sc alloys show a

narrower temperature range of the effective hardening between 300 °C and 350 °C and almost no hardening can be observed above 450 °C. The ternary Al-Sc-Zr alloy gain the hardness in the temperature range between 350 °C and 450 °C. Recent works reported a formation of complex Al_3(Sc,Zr) coherent precipitates with the core enriched in scandium [25]. This can explain the accelerated hardening in ternary alloys as compared to binary alloys. Scandium difuses in aluminum faster than zirconium and forms clusters, which then act as nucleation sites for the Al_3(Sc,Zr) phase.

Cieslar et al. [26] studied the influence of Sc and Zr on properties of TRC Al-Mg alloy. Maximal hardening of the material during an isochronal annealing experiment was obtained after annealing at 350 °C (see Figure 1.1). Microhardness distribution together with corresponding pictures of the material structure viewed by light optical microscope in polarized light are shown in Figure 1.2. StrengtheningAl_3(Sc,Zr) precipitates have two roles. Firstly, they harden the material after annealing at medium temperatures around 300 °C, and at higher temperatures they cause the pinning of grain boundaries and hinder recrystallization.

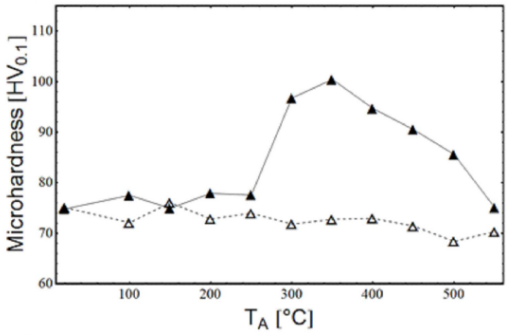

Figure 1.1: Microhardness evolution during isochronal annealing experiment of Al-Mg (empty symbols) and Al-Mg-Sc-Zr (full symbols) alloys [27].

Figure 1.3 shows the results of isothermal annealing experiments. Precipitation hardening effect of Al_3(Sc,Zr) particles was also confirmed. The highest increase of the microhardness was observed after annealing at 300 °C. Moreover, the precipitates diameter was smaller than the one after annealing at 350 or 400 °C which ensures higher pinning force acting against recrystallization. The maximal values of microhardness were obtained already after two hours at 300 °C. No improvement of microhardness was observed after further annealing [27]. However, due to a large-scale of industrial production the use of longer annealing times is desired. It was shown that no deterioration of properties occurred even after 8 h of annealing. Therefore, annealing 300 °C / 8 h was chosen for further investigation.

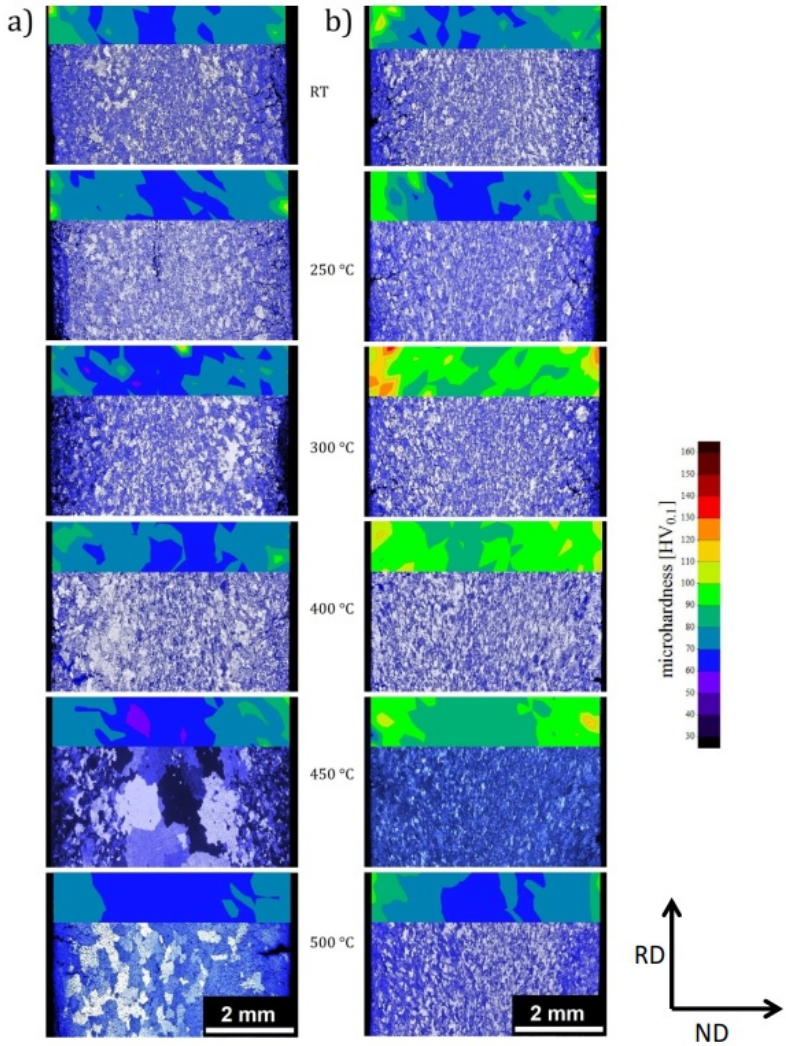

Figure 1.2: Difference in microstructure and microhardness profile along the sample cross-section during isochronal annealing of Al-Mg alloy without (a) and with (b) addition of Sc and Zr.

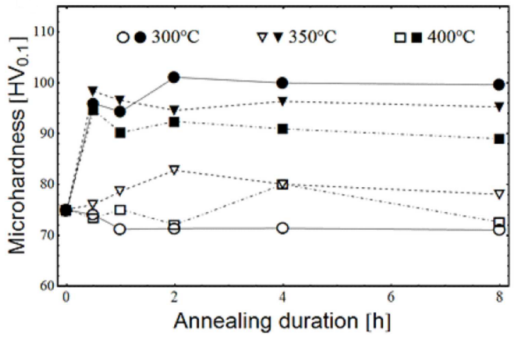

Figure 1.3: Microhardness evolution during an isothermal annealing experiment of Al-Mg (empty symbols) and Al-Mg-Sc-Zr (full symbols) alloys [27].

1.3 Twin-roll casting

Twin-roll casting (TRC) is a modern and effective casting method designed to metal sheets and strips production. Compared to a conventional direct chill casting (DC), TRC has a higher solidification rate that causes a higher supersaturation by Mg atoms. The high solidification rate leads to a homogeneous distribution of alloying elements that could not be reached by conventional casting methods [28, 29].

Principle of TRC is shown in Figure 1.4. Molten metal is poured between two cooled, rotating rolls. Between them the melt solidifies, is immediately subjected to a rolling process, and undergoes a plastic reduction. As a result, the strip of a final thickness is obtained.

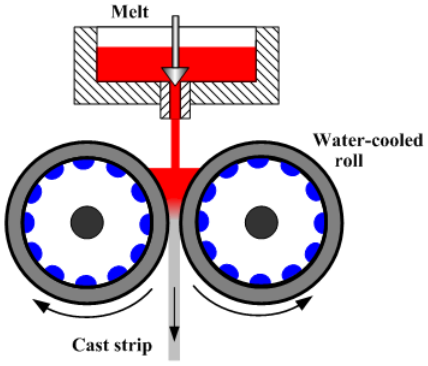

Figure 1.4: Scheme of TRC casting with a vertical rolling plane [30].

The microstructure of a TRC strip is rather homogeneous and equiaxed, the grain size is larger than the one obtained by a DC casting and rolling (Figure 1.5). That feature strongly influences the strength of the material. Mathematically, it is described by a Hall-Petch relation [31]

$$\sigma = \sigma_0 + Kd^{-1/2}, \tag{1.6}$$

where σ is strength, d is the grain size and σ_0 and K are material constants. Strength of the material increases with a decreasing grain size. Ductility usually decreases as the microstructure is finer. An optimal grain size range, where the particular material would have both high strength and good ductility, should be established for structural applications.

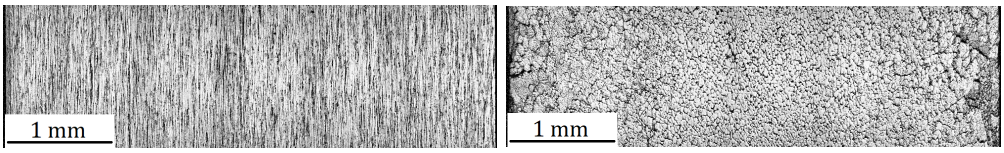

(a) Direct chill cast material (b) Twin roll cast material

Figure 1.5: Light optical micrographs of as-cast materials.

However, also TRC has several disadvantages – a centerline segregation [32, 33] causing the cracking or worsening of mechanical properties like formability, corrosion resistance and hardness of the strip.

1.4 Equal channel angular pressing

To reach the desired properties of a final product, severe plastic deformation (SPD) methods can be applied [34]. Possible examples of SPD methods suitable for metal sheets processing are asymmetric rolling (ASR) [35], accumulative roll bonding (ARB) [36], equal channel angular pressing or rolling (ECAP or ECAR) [37, 38], constrained groove pressing or rolling (CGP or CGR) [39, 40]. Nevertheless, both ARB and ASR bring the same problems as the ones exhibited by the conventional casting method. The grains are flat and elongated in the rolling direction. With these methods the pancake structure typical for conventional methods could not be avoided. Microstucture after CGP and ECAP is, on the contrary, equiaxed and therefore they might be very promising thermomechanical treatments [41].

A subject of this work is a description of an influence of ECAP on the microstructure and mechanical properties of TRC Al-Mg-Sc-Zr alloy. Scheme of the procedure can be seen in Figure 1.6a. A metal billet is extruded through a right angle channel. The process could be repeated untill the optimal state is obtained, and of course, it is possible to rotate the billet and perform each pass in different directions. Obviously, ECAP is not suitable for sheets, so ECAR as a modification of ECAP was later developed [37,38]. Feeding the workpiece using the feeding roll (shown in Figure 1.6b) instead of feeding the material using the hydraulic press makes continuous operation possible and allows the formation of various metal strips of desired final dimensions. Nevertheless, the changes in the microstructure after an application of both methods are comparable, so the investigation of the material properties could be carried out by either of them.

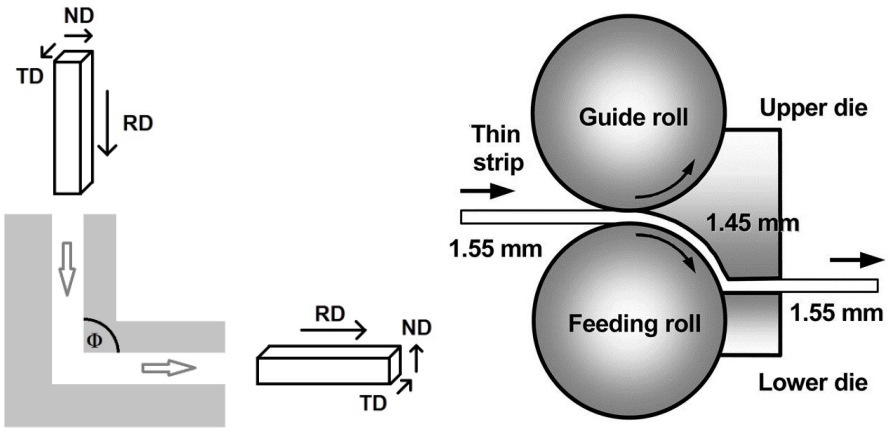

(a) ECAP (b) ECAR

Figure 1.6: Schemes of equal channel angular pressing and rolling

2. Material

Al-Mg strips with Sc and Zr addition were twin-roll cast at the University of Paderborn [42]. The experimental twin-roll caster is equipped with two rolls, which are water-cooled from inside. Diameter of the rolls is 370 mm and the length is 200 mm. The maximal casting rate is 8 m/min.

Table 2.1: Chemical composition of Al-Mg-Sc-Zr alloy in wt.%

	Al	Mg	Zr	Sc	Mn	Si	Cu	Fe
Composition	Balance	3.24	0.14	0.19	0.16	0.11	0.024	0.21

The alloy was melted in a resistance furnace with mechanical stirring. Molten metal was than poured between rotating rolls. Parameters of casting are displayed in Table 2.2. Casting process was realized with a vertical operation plane. Neither before nor during the process lubricant agents were applied on the roll surface.

Table 2.2: TRC parameters

Parameter		
Melt temperature	655	°C
Casting rate	2.75	m/min
Strip thickness	5.0	mm
Cooling water's flow rate	115	l/min

Twin-roll casting with the parameters mentioned above enables the preparation of the strip with a final thickness of 5 mm. Surface quality of the as-cast Al-Mg strip is shown in Figure 2.1.

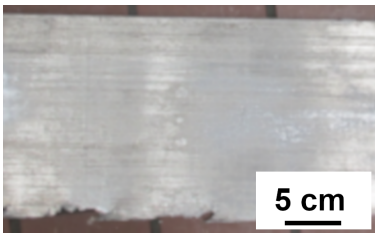

Figure 2.1: As-cast Al-Mg-Sc-Zr strip

Due to superior features of Al-Mg-Sc-Zr the influence of further treatment was studied. A billet prepared from the strip was subjected to equal channel angular pressing, which was performed four times at 250 °C, the dimensions of the extruding channel were 5 × 5 mm^2 and pressing speed was 10 mm/min.

Several samples were annealed at 300 °C for 8 hours before the annealing experiment (and before or after ECAP) in order to form coherent particles Al_3(Sc,Zr) with the strengthening effect. The influence of severe plastic deformation and effect of precipitation hardening were studied.

3. Experimental methods

3.1 Microhardness measurement

Similarly as for light optical microscopy and EBSD analysis bulk samples were prepared for microhardness measurement. Samples of a size of about 0.3 × 0.5 × 0.5 cm^3 were cut by Struers circular saw. Following steps are different for each of experimental methods.

Samples were embedded in an acrylic cold mounting resin ClaroCit for microhardness measurements. After curing of the resin, the samples were mechanically grinded and polished using diamond suspension with the last suspension containing diamond particles with the size of 1 μm .

Polished resin cylinders containing specimens were fixed in a holder. The microhardness measurements were performed by the Vickers method with a fully-automated hardness tester Qness Q10. Diamond indentor of pyramidal shape is impressed into the material with a precisely defined loading. Size of the indentantion area A is converted to the hardness value HV

$$HV = F/A \approx \frac{1.854F}{d^2}, \tag{3.1}$$

where d is the diagonal of the indentation, F the loading force.

Loading 100 g and dwell time 10 s were used in the experiment. At least 10 indents on each sample were performed to calculate the average value of microhardness.

3.2 Light optical microscopy

Light optical microscopy (LOM) in polarized light was used in order to receive global information about the material microstructure. The same samples as for microhardness measurement were used. Anodization by Barker's reagent (1.8% solution of fluoboric acid in water) resulting in the deposition of a film of Al_2O_3 on the surface [43]. The thickness of the film formed on each particular grain depends on the grain orientation and causes different rotation of the plane of light polarization. Black and white contrast of the grain structure can be seen when the light passes through the analyzer. Final image can be colored if a sensitive tint plate is added [44–47].

Good results were obtained after anodization performed at 15 °C using the voltage 20 V. The procedure lasted 4 min.

3.3 Electron backscatter diffraction

Electron backscatter diffraction (EBSD) is a method based on a Kikuchi lines analysis in scanning electron microscopy [48]. A large amount of inellastically back scattered electrons is generated in all directions. Some of the directions can meet the Bragg conditions of the particular grain so that electrons propagating in that direction can be scattered elastically. Directions, where the Bragg conditions

are fulfilled, create two cones. The EBSD detector detects the Kikuchi pattern as intersecting lines of the cones and the detector area [49]. Kikuchi patern is very sensitive to a crystal orientation – even a small tilting angle causes notable shift of the pattern.

Because the sample surface is scanned by the electron beam, the Kikuchi patern is created and analyzed point by point. The basic result of this method is a map of crystal orientations of the selected area on the sample surface.

Samples of the size of about $1 \times 0.5 \times 0.5$ cm^3 were cut by a circular saw. The specimen surface was subsequently mechanically grinded on SiC papers followed by a mechanical polishing using a diamond suspension. Finally, the polished section was electropolished in LectroPol-5 at –19 °C using a 30% solution of HNO_3 in methanol with a voltage of 10 V. Time of electropolishing was 3 s.

The analysis was performed using a Quanta 200F scanning electron microscope with accelerating voltage 10 – 15 kV. The studied surface was perpendicular to the transversal direction (TD) of the sample. Acquired data were subjected to standard clean-up procedures. Low angle grain boundaries with misorientation 5° – 15° and high angle boundaries with misorientations above 15° were highlighted with white and black line, respectively. The grain size was evaluated by EDAX OIM Analysis^{RM} software [50].

3.4 Transmission electron microscopy

Transmission electron microscopy (TEM) enables to reveal finer features of the material microstructure. Accelarated electrons propagate through a thin specimen and interact with atoms in the crystal lattice. TEM can work as a microscope or as a diffractograf depending on the plane where a projective system is focused. Conventional selected area diffraction or Kikuchi line pattern of a particular grain can be obtained if the projector is focused on the back focal plane.

In the imaging mode two main techniques were used – bright field (BF) and dark field (DF) imaging. The difference is in the selection of the electron beam which goes through the objective aperture. In a thin part of the specimen, particularly the Bragg-scattered electrones contribute to the image contrast. More details about TEM imaging modes and electron diffraction can be found in [51,52].

Samples for TEM observation were sliced by a circular saw. The initial thickness was around 0.5 mm. Then, specimens were thinned mechanically on SiC grinding papers to the thickness of 0.15 mm. After these procedures 3 mm targets were punched and electrochemically thinned at Tenupol-5 at –19 °C in 33% solution of HNO_3 in methanol.

Specimens were observed in transmission electron microscope JEOL JEM 2000FX with accelerating voltage 200 kV.

4. Results

4.1 Microhardness

The twin-roll cast Al-Mg-Sc-Zr alloy was submitted to two types of treatments – severe plastic deformation by ECAP and precipitation annealing. For the basic evaluation of mechanical properties, the Vickers microhardness was measured during isochronal annealing experiment. All three deformed samples were compared to both the as-cast state and the annealed state at 300 °C for 8 h. The same isochronal step by step heating scheme as in [27, 53] was used – all samples were annealed up to 600 °C with the step of 50 °C / 50 min. After each step samples were quenched into water.

4.1.1 Initial states

The initial value of the microhardness of the as-cast material, (78 ± 10) HV, was the lowest one observed in all samples. Annealing at 300 °C / 8 h raised the microhardness to (92 ± 3) HV. The maximum value (111 ± 16) HV was reached in the deformed material. Additional annealing of deformed samples either before or after ECAP leads always to a decrease of microhardness, (102 ± 3) HV for the post-ECAP annealed sample and (100 ± 4) HV for the material annealed before ECAP.

4.1.2 Isochronal annealing

Microhardness evolutions of all studied materials during isochronal annealing are depicted in Figure 4.1. Microhardness of the as-cast material (Figure 4.1a) started at (78 ± 10) HV and remained constant up to 250 °C. Then a sharp increase followed and the maximal value (100 ± 11) HV was reached at 350 °C. For a comparison microhardness of a non-deformed specimen annealed isothermally 350 °C / 8 h is shown. This strengthening is related to the precipitation of a fine dispersion of the Al_3(Sc,Zr) phase. The as-cast material, which was pre-annealed at 300 °C / 8 h, had been strengthened by Al_3(Sc,Zr) precipitates before the experiment. The microhardness was about (94 ± 8) HV up to 300 °C. A slight increase (however, within the limit of an experimental error) of the values up to (100 ± 6) HV was detected between 300 °C and 350 °C. Both of the non-deformed materials reached the same maximal value of the microhardness in the same temperature range.

As can be seen in the Figure 4.1b, deformation by ECAP brought even more strengthening into the material. Although the only deformed material by ECAP was the hardest at the beginning, anneling to 150 °C caused a significant drop of microhardness values. The hardenning effect caused in this material by ECAP was connected with a small grain structure (see further the results of LOM, EBSD, TEM) and higher dislocation density. Exposure of such a material to elevated temperatures usually results in the recovery and softening of the material, if they are not hindered by obstacles in the material. However, further annealing launched the precipitation, so the microhardness increased again to the initial

value of (110 ± 3) HV at 300 °C. The precipitation annealing, applied either before or after ECAP, had a stabilizing effect, because no drop of microhardness was measured as in the case of the only deformed material. The order of deformation and annealing resulted in lower microhardness of the pre-annealed and then ECAP-ed material.

Behavior of the samples at temperatures above 350 °C was very similar. Microhardness decreased as the precipitates coarsened during the annealing. It could be noticed that the microhardness of the non-preheated and deformed material steeply decreased between 500 °C and 550 °C, whereas the pre-heated samples exhibit similar decrease at temperatures between 550 °C and 600 °C. This difference could be a sign that the recrystallization of the deformed samples started earlier for non-annealed material due to a different distribution of $Al_3(Sc,Zr)$ phase.

However, it has to be mentioned that the measured differences of microhardness are subtle within the experimental scatter.

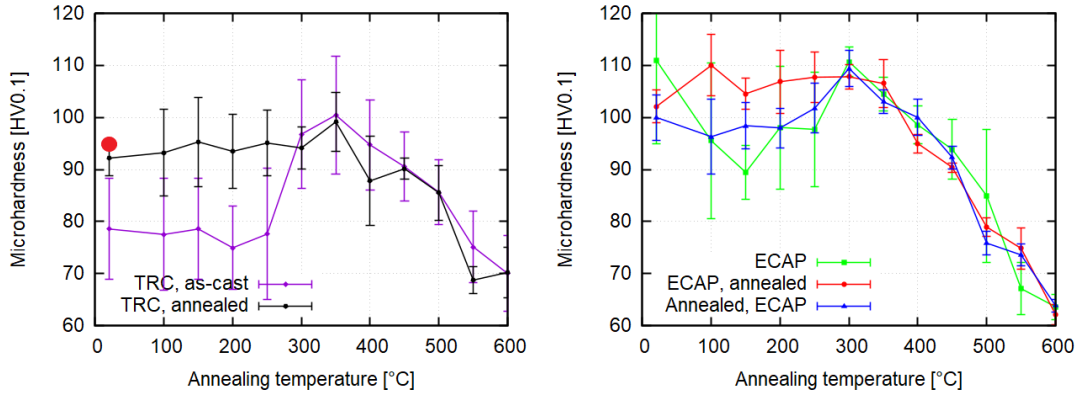

(a) TRC as-cast samples

(b) Samples deformed by ECAP

Figure 4.1: Microhardness evolution during isochronal annealing. Red circle shows the microhardness of the non-deformed TRC specimen annealed isothermally 350 °C / 8 h.

4.2 Light optical microscopy

4.2.1 Initial states

Light optical microscopy was used for the comparison of TRC and ECAP materials. Because this method provides an overwiev of the microstructure and could not provide a sufficient resolution to observe fine variations of the microstructure after several ECAP passes or after annealing of the initial TRC material, only two images of initial states from light optical microscope after TRC (Figure 4.2a) and after 4 ECAP passes (Figure 4.2b) are enclosed. A significant grain size reduction can be noticed in the sample subjected to ECAP in comparisson with the as-cast material.

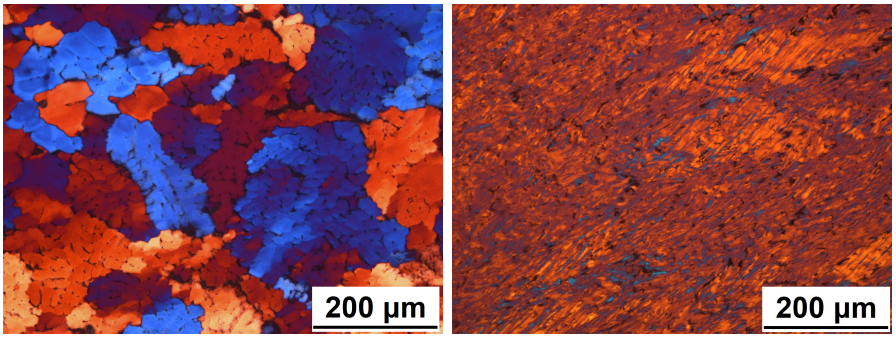

(a) TRC as-cast material (b) Material deformed by ECAP

Figure 4.2: Grain structure of initial states.

4.2.2 Isochronal annealing

Nevertheless, tiny variations of the microstructure could be responsible for significant changes in the final material structure. Six following figures show that the precipitation annealing has a considerable impact on the microstructure after recrystallization. Grains in the non-annealed deformed samples are coarser with an inhomogeneous distribution.

The microstructure evolution remained similar for both non-annealed (Figures 4.3a and 4.3b) and annealed (Figures 4.3d and 4.3e) ECAP processed materials during isochronal annealing up to 550 °C. The significant differences of the grain size was observed after annealing at 600 °C. The non-annealed material contained regions with coarser grains (see Figure 4.3c), while the microstructure of the annealed one was more homogeneous and the grain size was noticeably smaller (see Figure 4.3f).

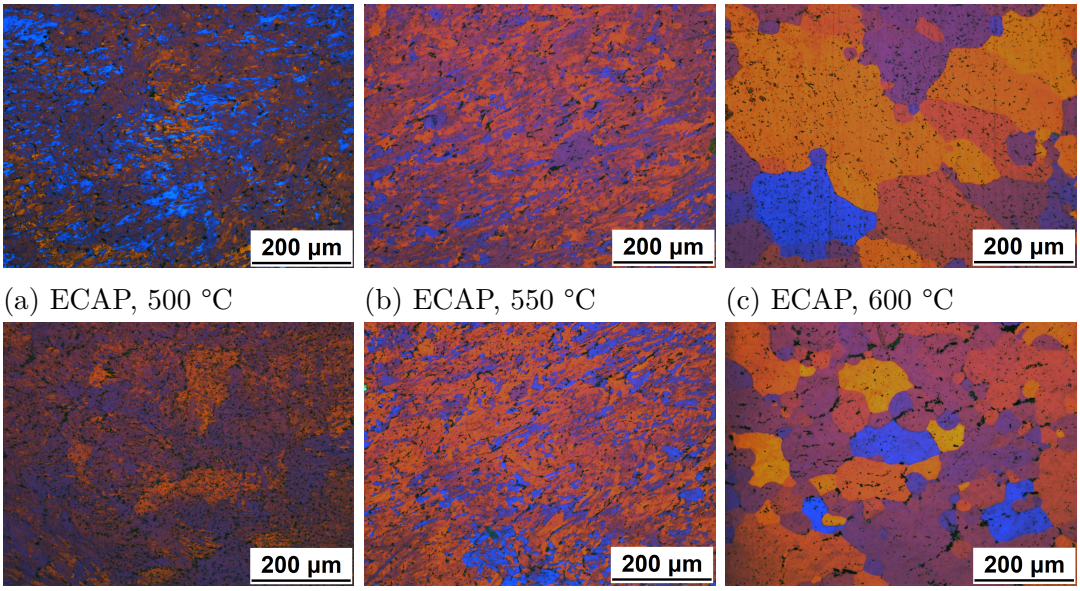

(a) ECAP, 500 °C (b) ECAP, 550 °C (c) ECAP, 600 °C

(d) ECAP, annealed, 500 °C (e) ECAP, annealed, 550 °C (f) ECAP, annealed, 600 °C

Figure 4.3: Grain structure of isochronally annealed specimens.

4.3 Electron backscatter diffraction

The grain distribution and orientation of the as-cast material and material processed by ECAP were studied by electron back-scatter diffraction. Samples were treated in the same manner as the ones used for the microhardness measurement. EBSD analyses were performed on initial states and states after selected annealing steps: 300 °C, 550 °C, 600 °C, which correspond with annealing temperatures connected with significant changes of the microhardness.

4.3.1 Initial states

The initial microstructure of the as-cast and the as-cast and pre-annealed samples are shown in the Figure 4.4. Annealing at 300 °C / 8 h probably caused not only $Al_3(Sc,Zr)$ precipitation but moreover a dislocations motion, so the grains are divided into small subgrains. Deformation by ECAP produced very fine grains slightly elongated in the direction of the extrusion (see Figure 4.5).

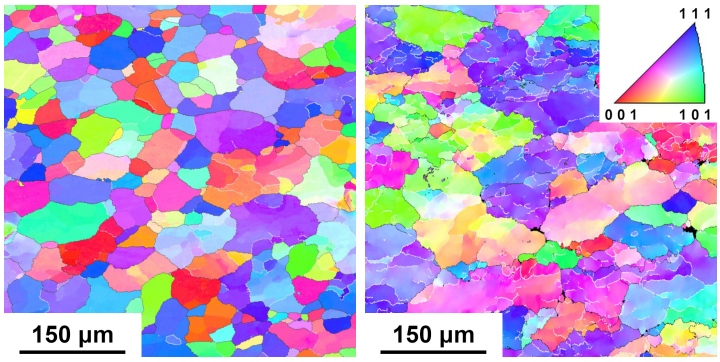

(a) TRC, as-cast (b) TRC, annealed

Figure 4.4: EBSD inverse pole figures of initial states of undeformed samples.

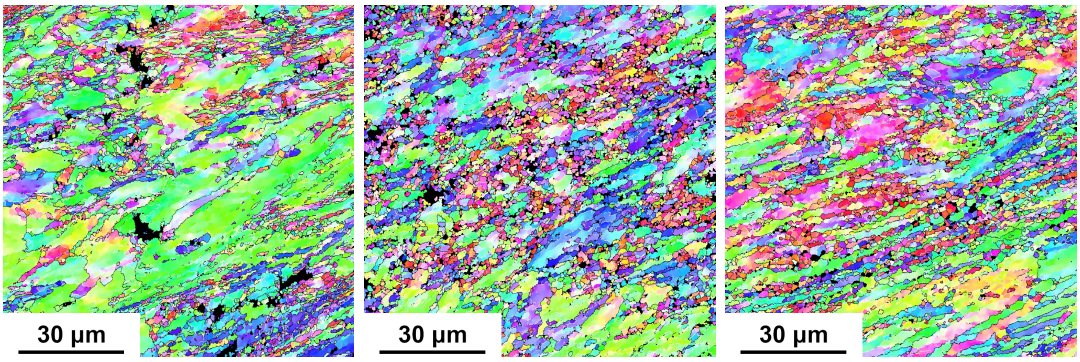

(a) ECAP (b) ECAP, annealed (c) Annealed, ECAP

Figure 4.5: EBSD inverse pole figures of deformed samples in initial states.

Due to a small grain size, it was necessary to choose a smaller step in EBSD, which influenced final size of the scanned region. The scanned region of non-deformed samples was 500 × 500 μm^2, whereas the size 100 × 100 μm^2 was selected for the deformed ones.

4.3.2 Isochronal annealing

The results of the EBSD analysis performed after isochronal annealing up to 300 °C did not show any remarkable changes in the microstructure. The only thing that can be noted is a slight decrease of misorientations within the grains.

Analysis of the states after the annealing up to 550 °C and 600 °C shows the progression of recrystalization. Significant fragmentation of grains into subgrains and partial recrystallization starting preferentially on high angle grain boundaries were observed in both as-cast and pre-annealed TRC materials (Figure 4.6).

Grains in the ECAP-ed material grew noticeably after annealing up to 550 °C. Their size was about four times larger than the one observed in the initial states (see Figures 4.7). However, 550 °C is not a sufficiently high temperature to introduce full recrystallization, and large areas exhibiting only recovery were observed in all specimens.

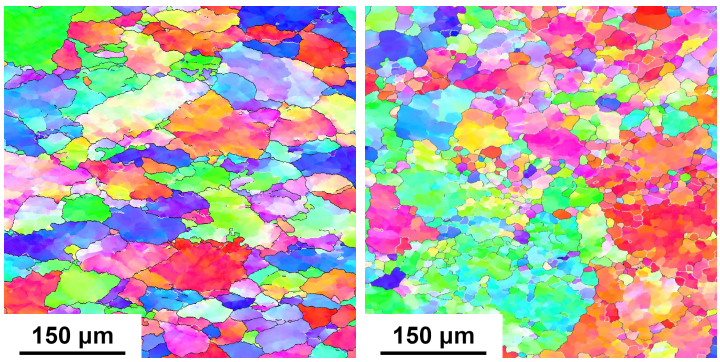

(a) TRC, as-cast (b) TRC, annealed

Figure 4.6: EBSD inverse pole figures of as-cast samples after isochronal annealing up to 550 °C.

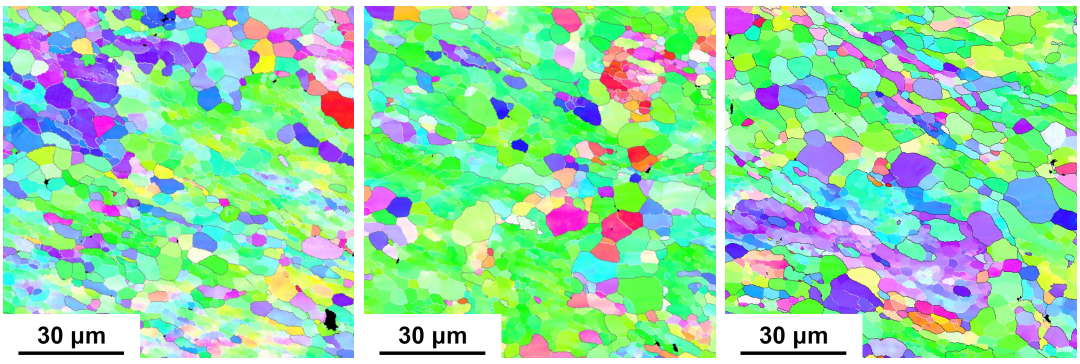

(a) ECAP (b) ECAP, annealed (c) Annealed, ECAP

Figure 4.7: EBSD inverse pole figures of deformed samples after isochronal annealing up to 550 °C.

Full recrystallization does not occur even at 600 °C in non-deformed materials (see Figure 4.8). Significantly higher recrystallized volume was observed in the material without pre-annealing.

Due to the significant grain growth at 600 °C in deformed samples, the analysis was performed in the region of 1000 × 1000 μm^2. The average grain size

increased about ten times. The microstructure difference between individual deformed samples is shown in Figure 4.9. The precipitation annealing before the experiment (both before and after ECAP) is responsible for the formation of obviously finer and more homogeneous grain structure after recrystalization which is in accordance with light optical microscopy observations.

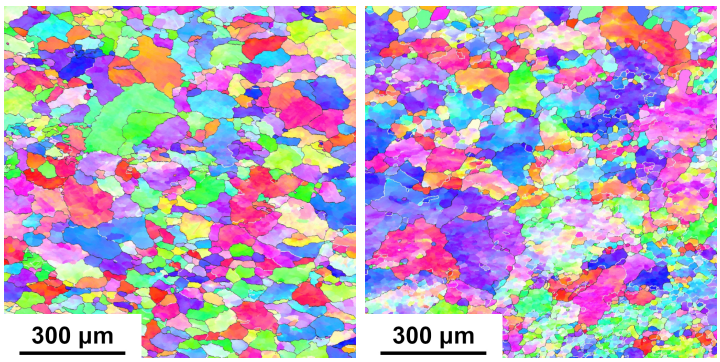

(a) TRC, as-cast (b) TRC, annealed

Figure 4.8: EBSD inverse pole figures of undeformed samples after isochronal annealing up to 600 °C.

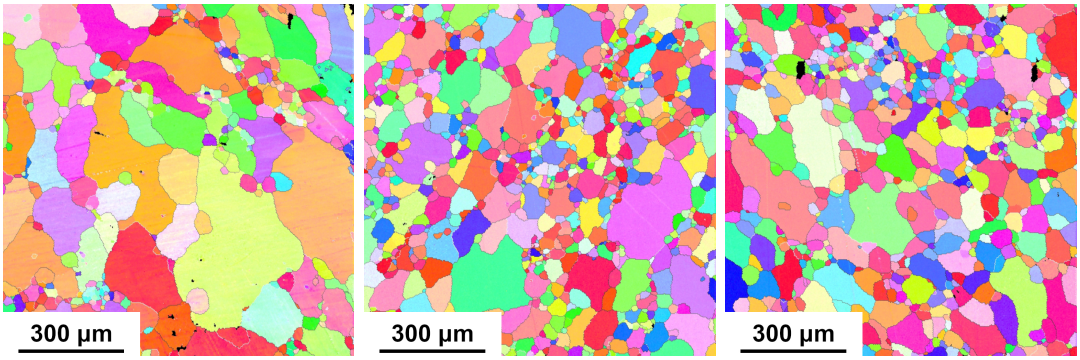

(a) ECAP (b) ECAP, annealed (c) Annealed, ECAP

Figure 4.9: EBSD inverse pole figures of deformed samples after isochronal annealing up to 600 °C.

Distribution of coherent areas diameters (areas divided by high-angle boundaries) are shown in Figure 4.10. A positive influence of ECAP on grain refinement was confirmed. The only observed effect of ECAP on the microstructure after annealing up to 600 °C is an intensification of recrystallization. A tendency to form a bimodal grain size structure was observed in all ECAP processed specimen. However, this disposition is more pronounced in the non-annealed sample.

4.3.3 Grain size distribution

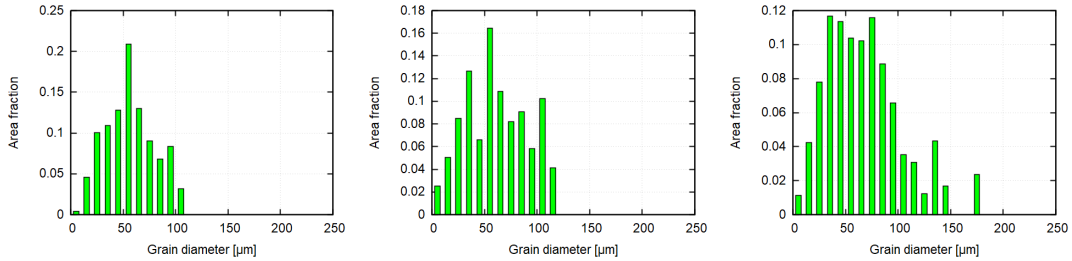

(a) TRC, as-cast, RT (b) TRC, as-cast, 550 °C (c) TRC, as-cast, 600 °C

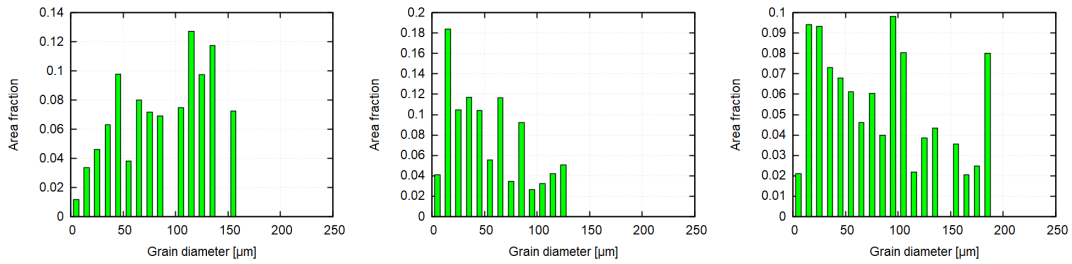

(d) TRC, annealed, RT (e) TRC, annealed, 550 °C (f) TRC, annealed, 600 °C

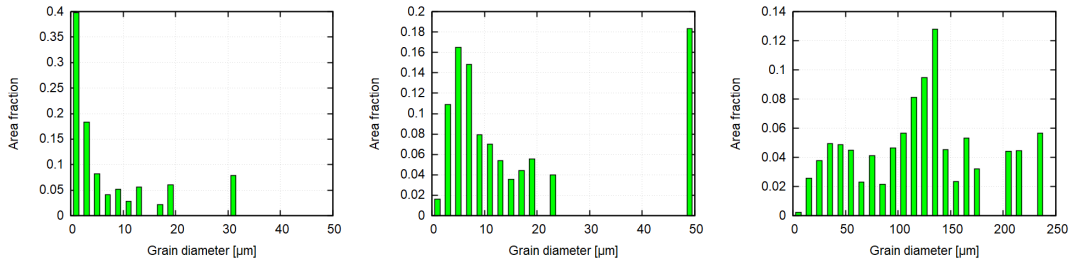

(g) ECAP, RT (h) ECAP, 550 °C (i) ECAP, 600 °C

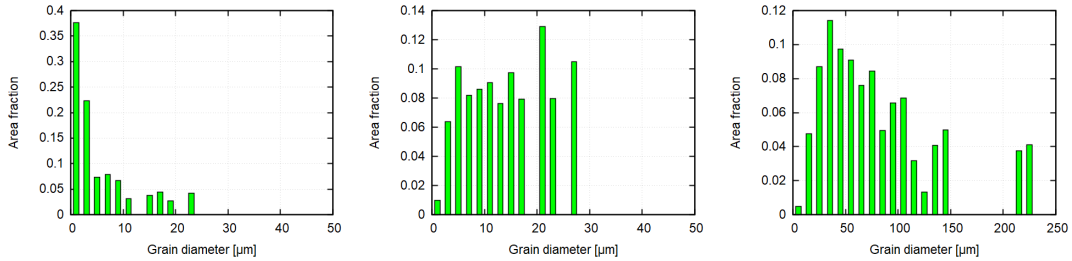

(j) ECAP, annealed, RT (k) ECAP, annealed, 550 °C (l) ECAP, annealed, 600 °C

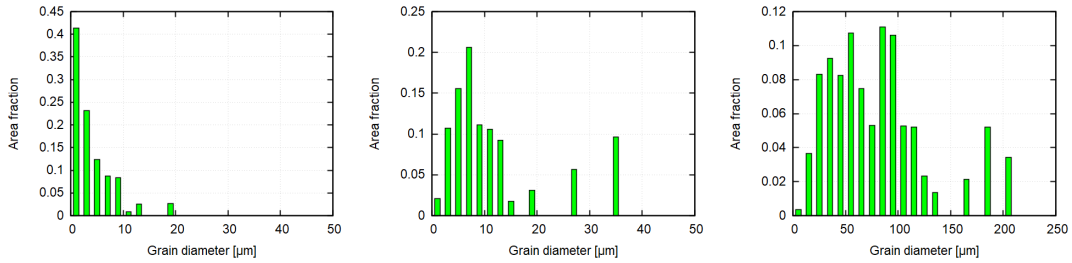

(m) annealed, ECAP, RT (n) annealed, ECAP, 550 °C (o) annealed, ECAP, 600 °C

Figure 4.10: Grain size distribution.

There are several definitions, how the mean grain size can be evaluated. Fitting of the grain size distribution by conventional lognormal function cannot be used due to a polymodal character of some distributions [54]. Therefore, the mean grain size was determined from the average intercept length L. Additionaly, it was assumed that the grain shape is approximated by a Poisson-Voronoi construction [55, 56], so the mean grain size d is

$$d = 1.445L. \tag{4.1}$$

The grain intercept length was evaluated by the automated procedure of the used OIM Analysis software, where grain boundaries were defined by misorientation angles greater than 5°. The mean intercept length was converted using equation 4.1 to the average grain size. Values of the average grain sizes are presented in the Table 4.1. Due to a limited statistics and inhomogeneous structure an average scatter of the values is about 10 – 15 % and larger than 30 % in bimodal structures.

Table 4.1: The average grain size [μm]

Sample	TRC	TRC + A	ECAP	ECAP + A	A + ECAP
RT	39	54	1.7	1.8	1.8
550 °C	28	22	6.6	10	6.7
600 °C	36	19	75	48	51

4.4 Transmission electron microscopy

4.4.1 Initial states

Dislocation substructure and other subtler details like precipitates or dispersoids of secondary phases were observed by TEM. Microstructure of the as-cast material is shown in Figure 4.11a. Dislocations form dislocation tangles inside equiaxed grains. Grain size is in the order of magnitude of hundreds μm, so just a small part of the grain could be seen in the Figure 4.11a. On the contrary, in the as-cast and annealed material, dislocations accumulate in dislocation walls and divide the grain into subgrains of several microns size (Figure 4.11b).

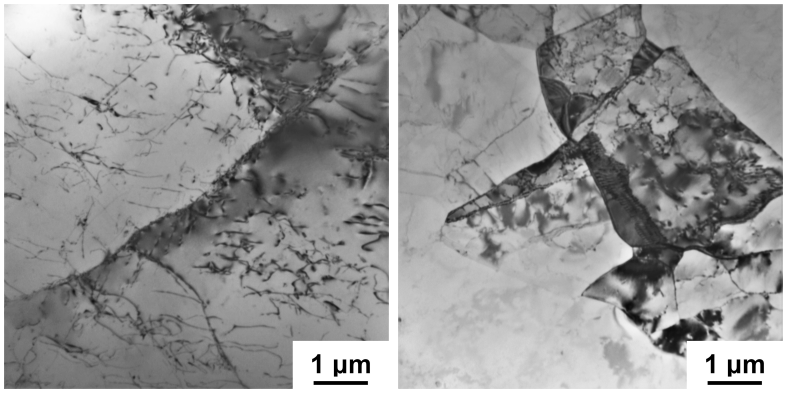

(a) TRC, as-cast (b) TRC, annealed

Figure 4.11: TEM images of initial microstructures.

Deformation by ECAP introduced a significant grain fragmentation. Grains are partially elongated in the shearing direction with the subgrain size of several hundreds of nanometers. Post-ECAP pre-annealing 300 °C / 8 h resulted in a slightly coarser structure of the material (Figure 4.12c) in comparison with the material deformed by ECAP without pre-annealing (Figure 4.12a) or material subjected to pre-annealing before ECAP(Figure 4.12b).

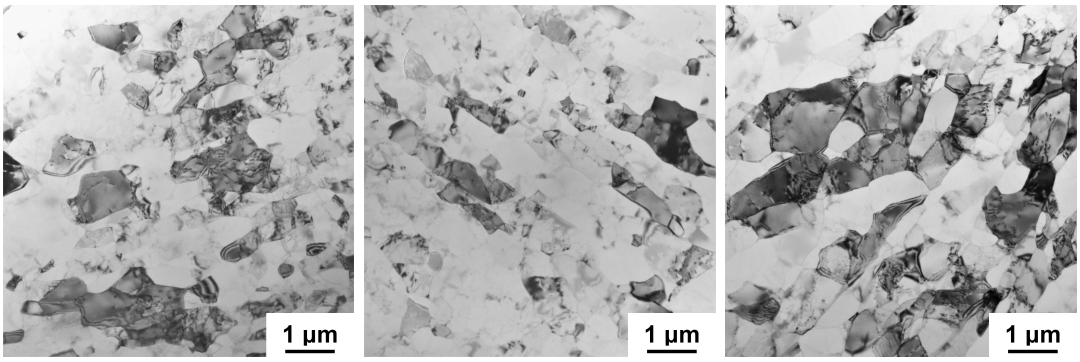

(a) ECAP (b) Annealed, ECAP (c) ECAP, annealed

Figure 4.12: TEM micrographs of ECAP processed samples.

Figure 4.13 was acquired at a higher magnification. Dislocations, subgrain and grain boundaries and the deformed microstructure of the samples after ECAP can be seen. Even in the bright field (in the Figure 4.13d both bright field and dark

field images are attached), the presence of fine $Al_3(Sc,Zr)$ precipitates could be confirmed in annealed samples – see the modulated intensity inside grains of the annealed specimens.

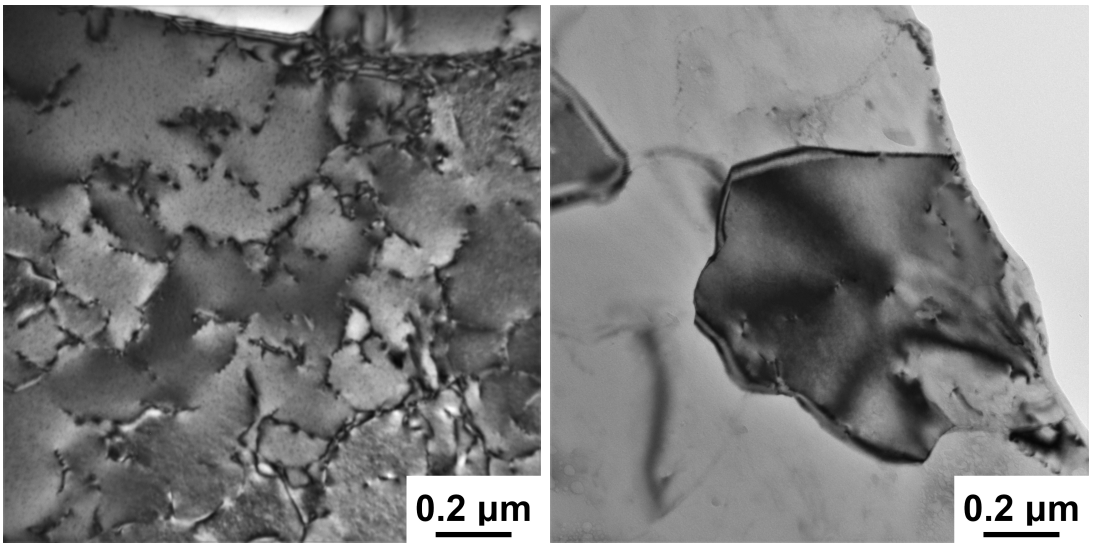

(a) TRC, annealed (b) ECAP

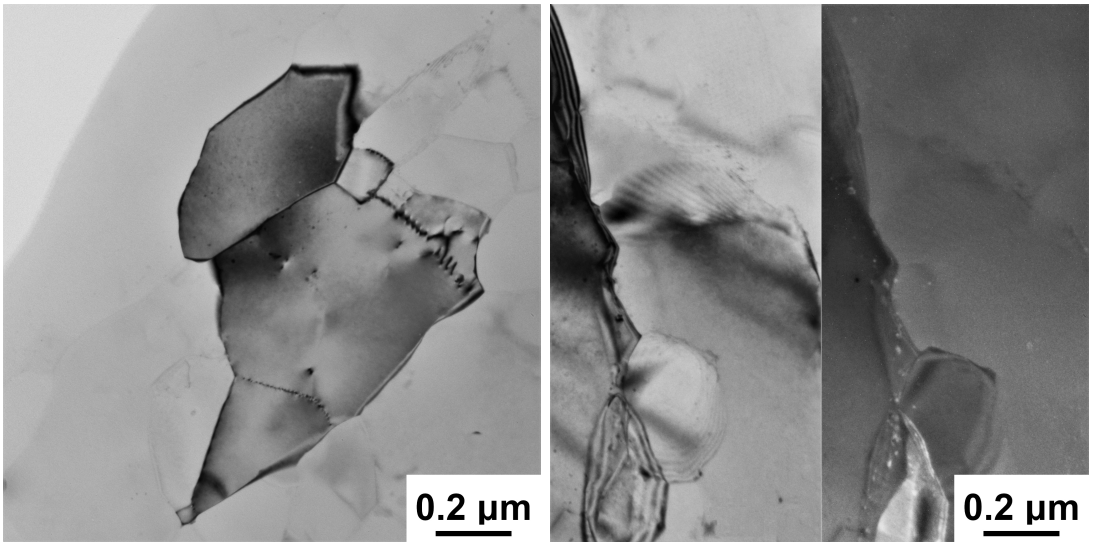

(c) Annealed, ECAP (d) ECAP, annealed

Figure 4.13: Detailed TEM images of the microstructures of TRC and ECAP samples.

Monitoring of the $Al_3(Sc,Zr)$ precipitates was performed specially in the dark field imaging mode near [001] crystal orientation in superstructural reflections belonging to $L1_2 - Al_3(Sc,Zr)$ ordered structure.

Presence of the $Al_3(Sc,Zr)$ precipitates was confirmed in all pre-annealed samples (see selected area diffraction patterns in Figures 4.14a, 4.14c, 4.14d). Due to a complexity of dark field observations of such small particles, convincing dark field images of these precipitates were acquired only in the non-deformed sample. Fine particles dispersed in Al matrix could be seen inside the grain (Figure 4.14a). Microstructure of the sample deformed before the precipitation annealing is shown in Figure 4.14d. The particles are coarser and situated often inside the

grain boundary. Similarly, observation of the precipitates in the dark field was rather unsuccessful in the specimen pre-annealed before ECAP. Therefore, bright field image with the same magnification is attached (Figure 4.14c). Nevertheless, inserted selected area diffraction (SAED) pattern contained superstructural reflections and also a modulated intensity inside the grain indicates the presence of $Al_3(Sc,Zr)$ phase.

The precipitates were not expected in the material subjected only to the ECAP without pre-annealing because the deformation was performed at 250 °C (material had been exposed to the temperature for a short time). SAED pattern belonging to the grain in the orientation [001] does not contain any superstructural reflections (see Figure 4.14b).

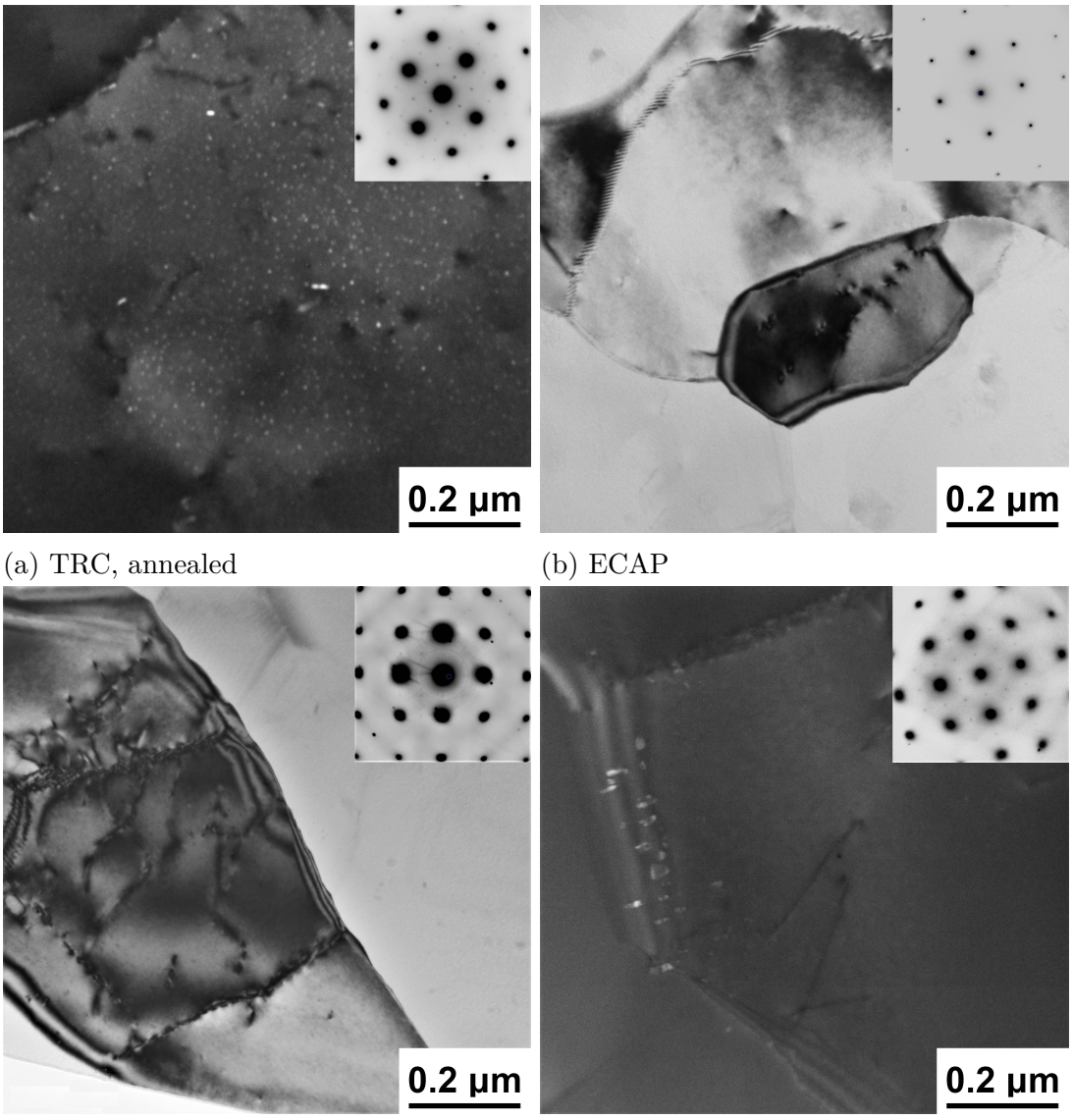

(a) TRC, annealed

(b) ECAP

(c) Annealed, ECAP

(d) ECAP, annealed

Figure 4.14: TEM micrographs of the $Al_3(Sc,Zr)$ distribution.

4.4.2 Isochronal annealing

Due to the rise of the microhardness in the temperature range between 200 °C and 350 °C, changes in the $Al_3(Sc,Zr)$ distribution were expected. Therefore, ECAP materials were subjected to the isochronal annealing up to 350 °C with the same heating scheme 50 °C / 50 min. Due to the focus of the thesis on materials after ECAP, TEM observations were not performed on isochronally annealed undeformed materials. For a rough estimation microstructures of undeformed specimens annealed at 350 °C / 8 h are shown in following images. This specimen is in accordance with Figures 4.15 and 4.16 marked as TRC, annealed*. The grain structures of the annealed materials are displayed in the Figure 4.15.

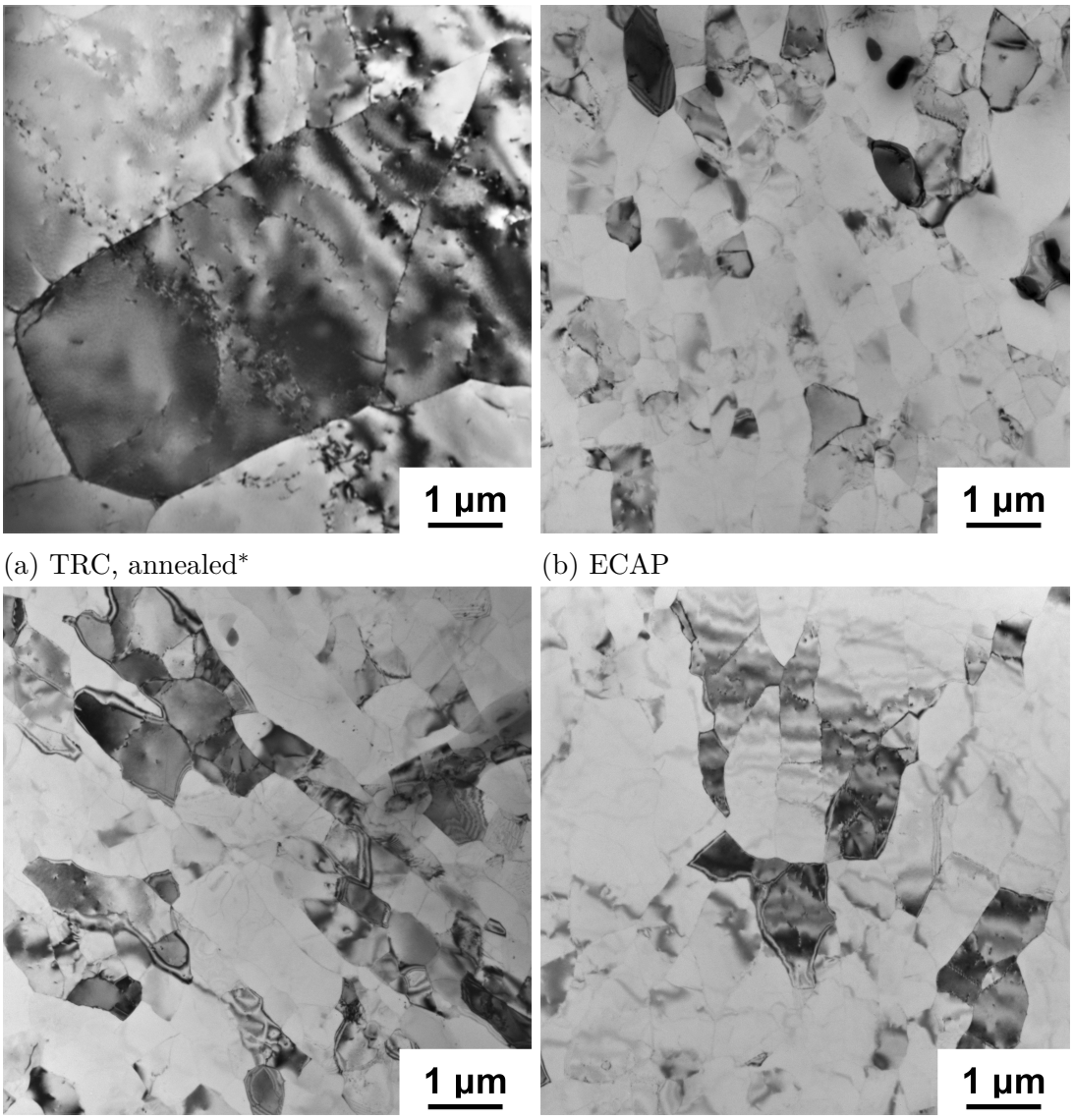

(a) TRC, annealed* (b) ECAP

(c) Annealed, ECAP (d) ECAP, annealed

Figure 4.15: TEM micrographs of specimens after isothermal annealing 350 °C / 8 h (a) and after isochronal annealing up to 350 °C (b-d).

No significant changes of the substructure were observed in isochronally annealed samples in comparison with initial states. The size of grains and subgrains remained the same. Subtler details of the microstructure were studied

using bright field imaging at higher magnification (Figure 4.16 a – d). Also dark field images of the Al_3(Sc,Zr) precipitates were received for all materials (Figure 4.16 e – h). A higher intensity of superstructural reflections in SAED patterns was detected. Fine precipitates were relatively uniformly dispersed in the matrix, small amount of the coarser ones decorated the grain and subgrain boundaries. Precipitates present in ECAP processed material were tinier than the ones in the non-deformed material. However, a different heating scheme should be taken into an account.

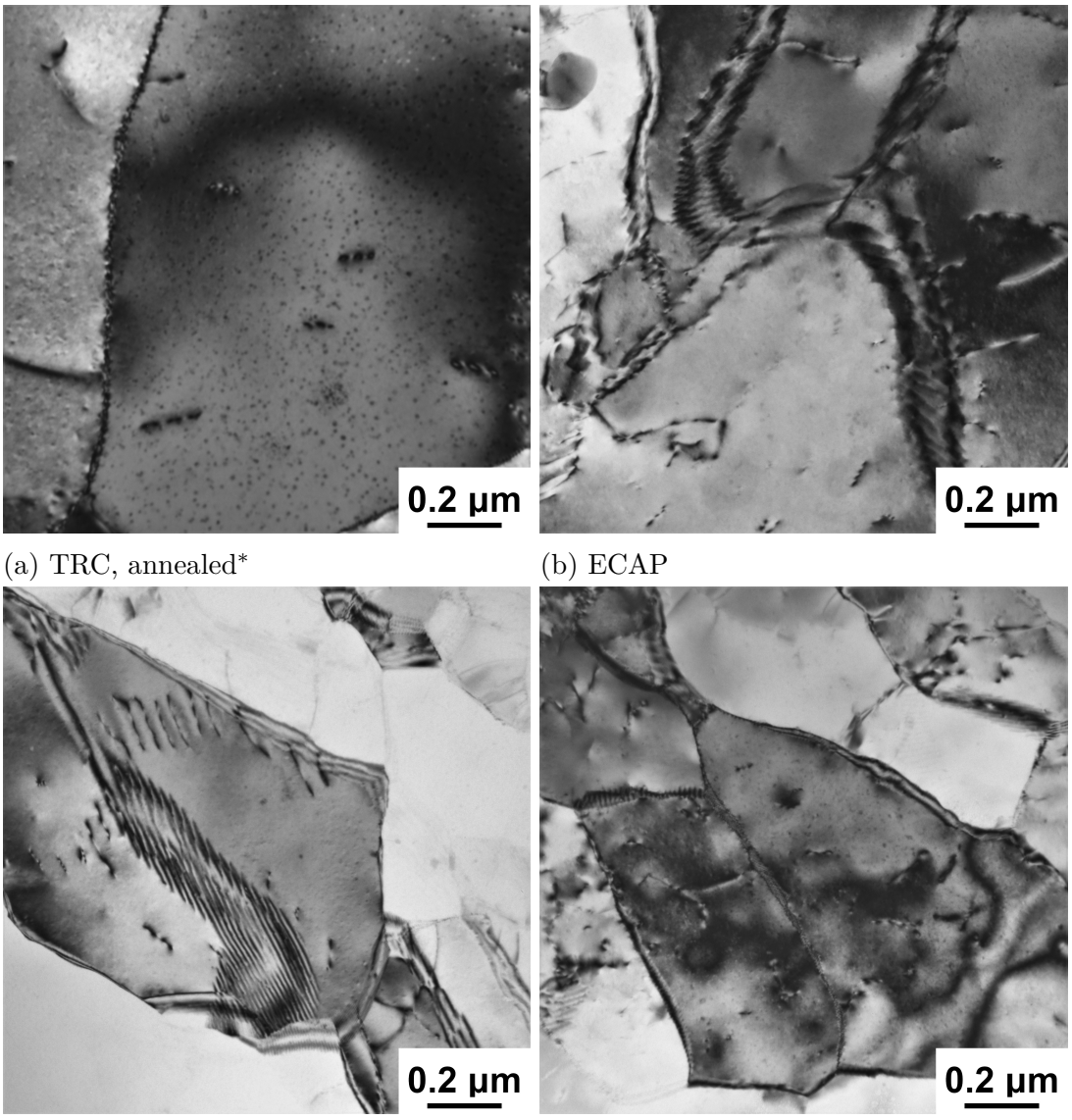

(a) TRC, annealed*

(b) ECAP

(c) Annealed, ECAP

(d) ECAP, annealed

Figure 4.16: TEM BF images of the Al_3(Sc,Zr) precipitates in specimens from Figure 4.15

Additional TEM micrographs displaying the Al_3(Sc,Zr) precipitates distribution in ECAP samples are attached in the Figure 4.18. Sample, that was not subjected to the 8 hours lasting pre-annealing, contained particles with a noticeable scatter in their size even inside the matrix. The preannealing 300 °C / 8 h

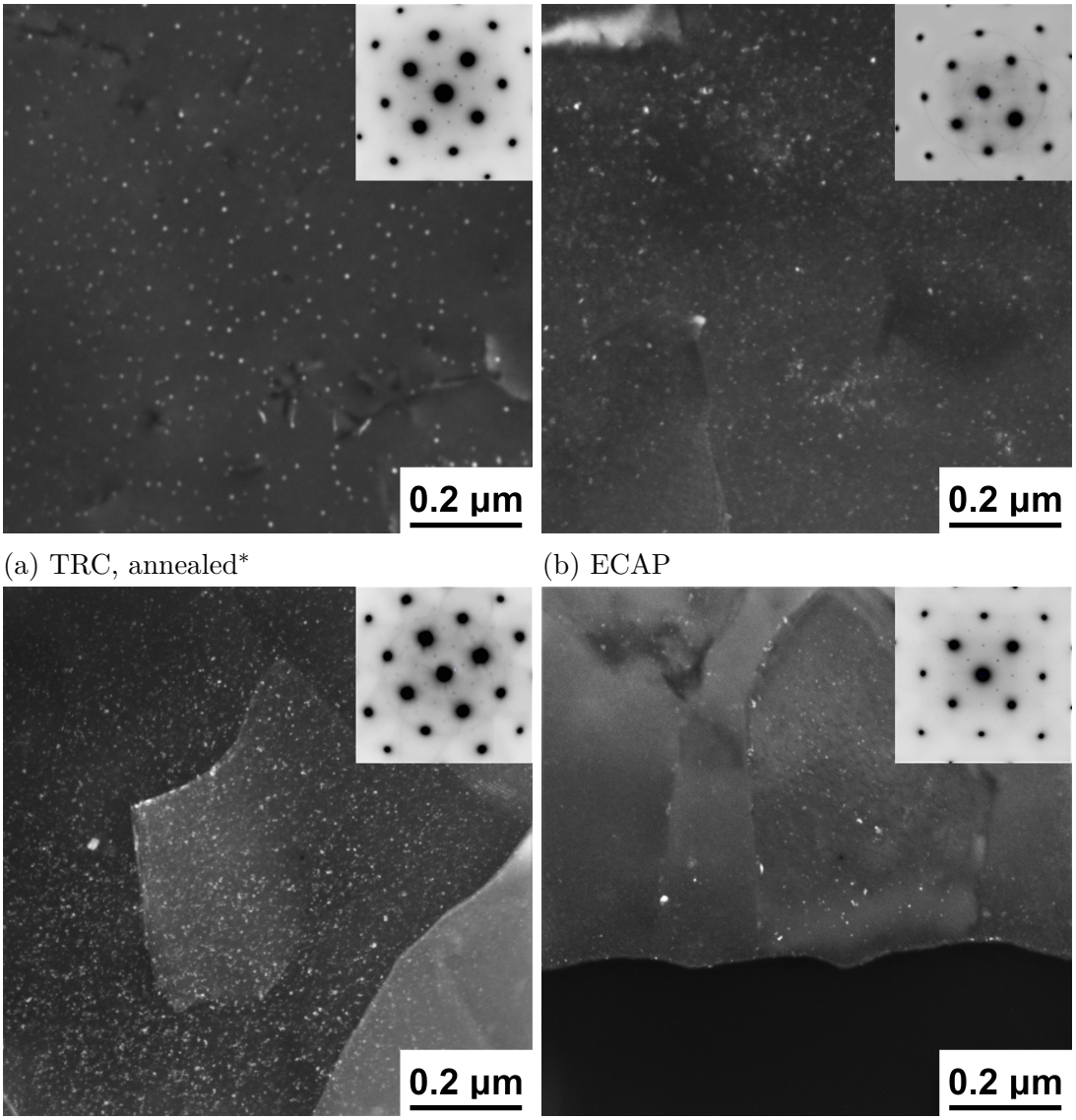

(a) TRC, annealed*

(b) ECAP

(c) Annealed, ECAP

(d) ECAP, annealed

Figure 4.17: TEM DF images of the Al_3(Sc,Zr) precipitates in specimens from Figure 4.15

led to more homogeneous Al_3(Sc,Zr) distribution, the differences were observed mainly between the particles dispersed in the matrix and those situated at subgrain boundaries.

The average size of the Al_3(Sc,Zr) precipitates was about 4 nm in ECAP processed samples isochronally annealed up to 350 °C (Fig. 4.23b). The average size of precipitates present in the non-deformed sample was about 6 nm – see Figure 4.23a).

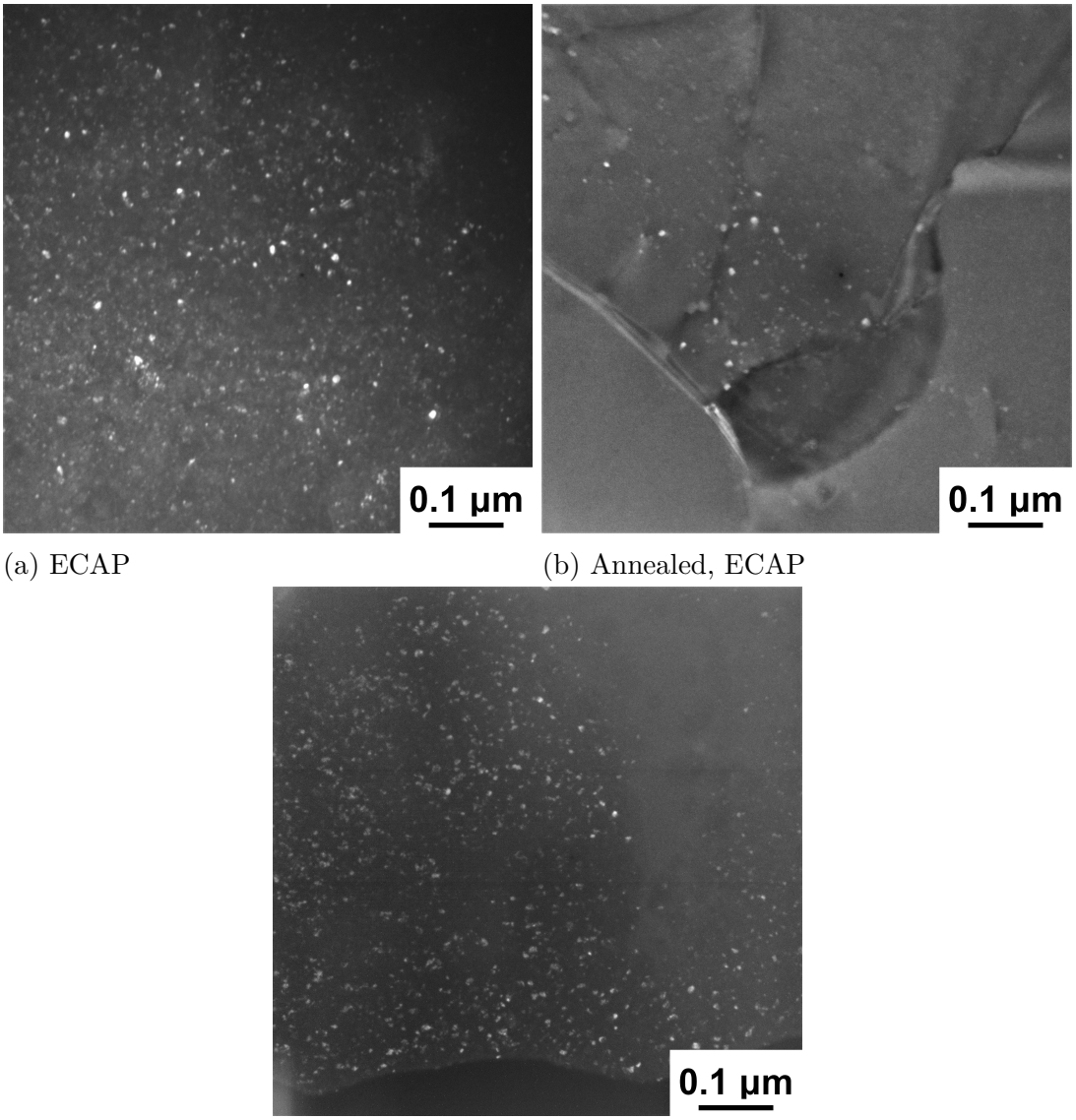

(a) ECAP

(b) Annealed, ECAP

(c) ECAP, annealed

Figure 4.18: TEM dark field micrographs of the $Al_3(Sc,Zr)$ dispersion in deformed samples after isochronal annealing up to 350 °C.

4.4.3 In-situ heating up to 550 °C

Microstructure of the ECAP material, that was not submitted to precipitation annealing before the experiment, was studied during in-situ annealing in transmission electron microscope. This method enables to observe microstructural changes directly during the heating procedure. The heating scheme 50 °C / 10 min was applied – the specimen was held 10 minutes at the required temperature, then the temperature was increased by 50 °C. These steps were done repeatedly up to 550 °C.

Our effort was to monitor the microstructural changes in one selected area at a rather fixed orientation. The observation was embarrassed by the thermal expansion of both the sample and the holder, therefore the specimen image shifting

and the sample tilt had to be adjusted on the fly during the heating.

The evolution of the microstructure is displayed in Figure 4.19 and 4.20. Probably, Al_6Mn particles arrised along the grain boundaries above 300 °C [57, 58]. Further annealing caused a growth of larger particles at the expense of smaller ones. Particles of Al_3(Sc,Zr) phase were for the first time assuredly confirmed at 450 °C. However, their presence at 350 °C and 400 °C could not be excluded due to a rather unappropriate orientation of observed grains (early stages of Al_3(Sc,Zr) phase formation could be observed in grains with [001] orientation parallel to the incident beam). Annealing up to 550 °C resulted in their coarsening. Size of the particles was measured at 450 °C, 500 °C and 550 °C. The average values are displayed in the Table 4.2.

Table 4.2: Size of Al_3(Sc,Zr) precipitates

Temperature [°C]	450	500	550
Size [nm]	(7 ± 2)	(9 ± 4)	(10 ± 4)

Also coarser rectangular and rod shaped particles were present in the matrix after annealing at 550 °C. According to [58] it could be $Al_{12}(Mn,Fe)_3Si$ phase.

The ultra-fine grain structure remained relatively unchanged even though the EBSD analysis (Figure 4.7 and 4.9) showed coarsening of the grains in deformed material after annealling at 550 °C in the air furnace. Therefore, EBSD analysis was performed also on the sample used for the in-situ heating experiment in TEM (Figure 4.21). The grain structure was entirely different. Near the edge of the TEM foil, part of the structure contained small recrystallized grains. Also partially deformed areas still persist near the edge of the hole after annealing up to 550 °C. Farther from the edge the grains were fully recrystallized and their size was comparable to the ones observed in the material annealed in the air furnace up to 600 °C. This heterogeneous structure was caused by the two-dimensional character of the thin TEM foil near the edge, where the grain coarsening was significantly constrained. The earlier recrystallization during the in-situ heating might be caused by a higher heating rate. Also the role of a thin specimen could not be neglected [59].

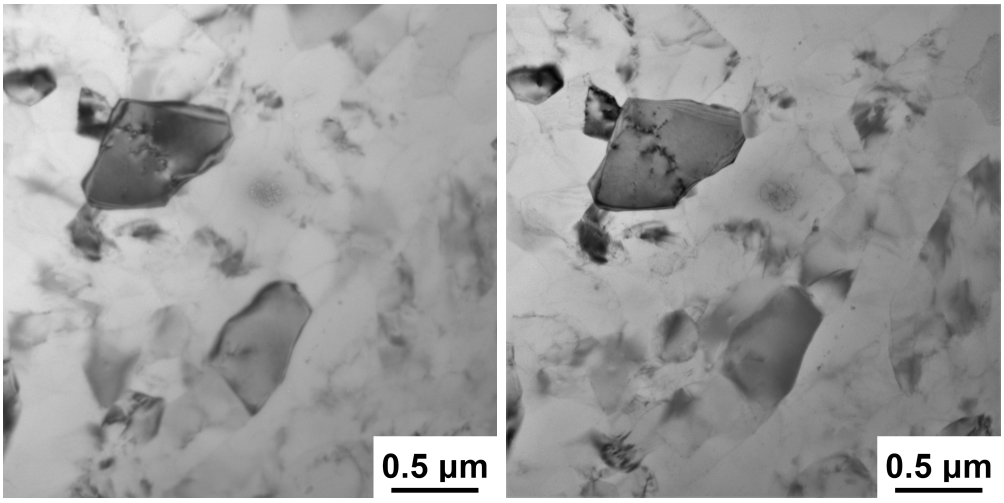

(a) RT (b) 100 °C

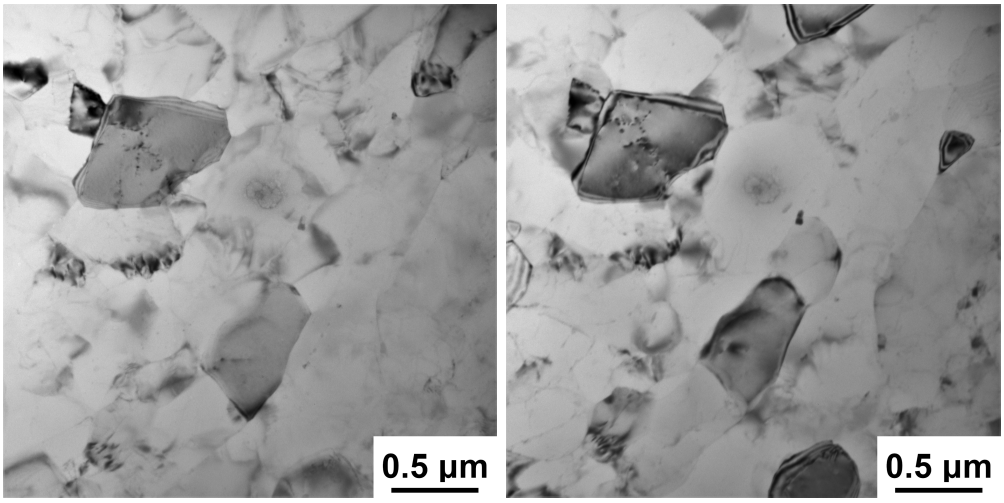

(c) 150 °C (d) 200 °C

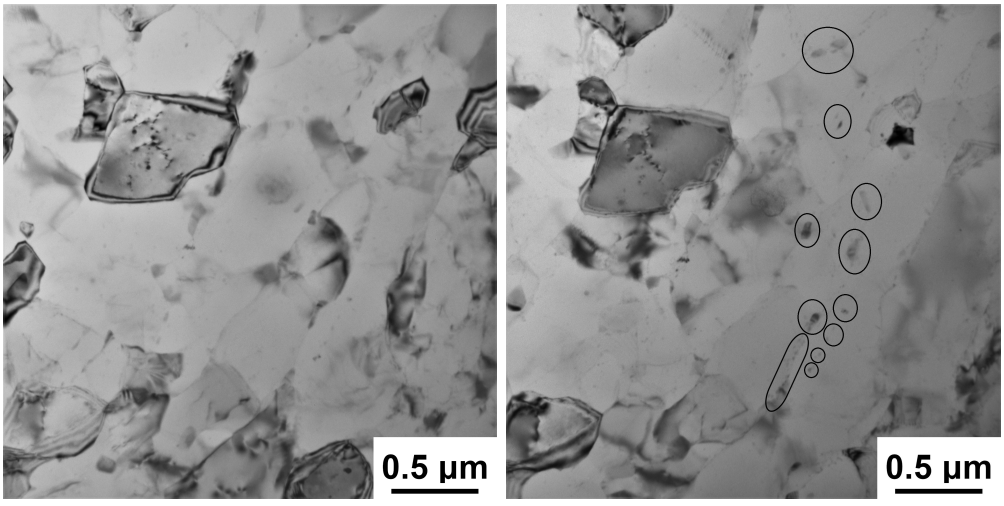

(e) 250 °C (f) 300 °C

Figure 4.19: In-situ TEM annealing of the specimen after ECAP. Black circles mark Al_6Mn phase.

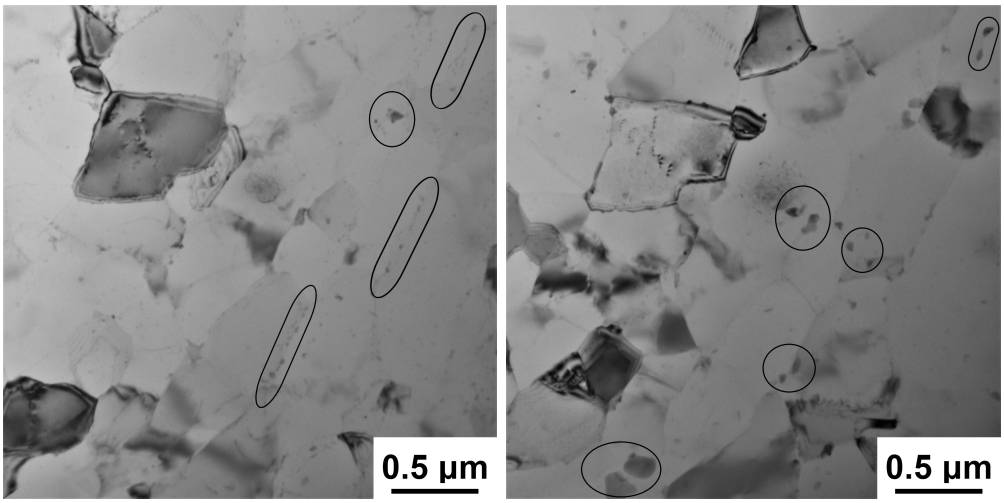

(a) 350 °C (b) 400 °C

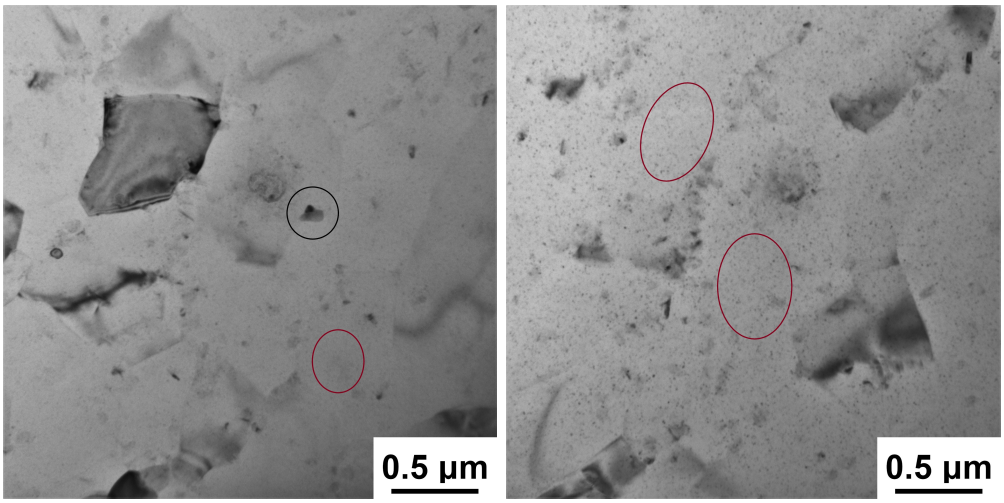

(c) 450 °C (d) 500 °C

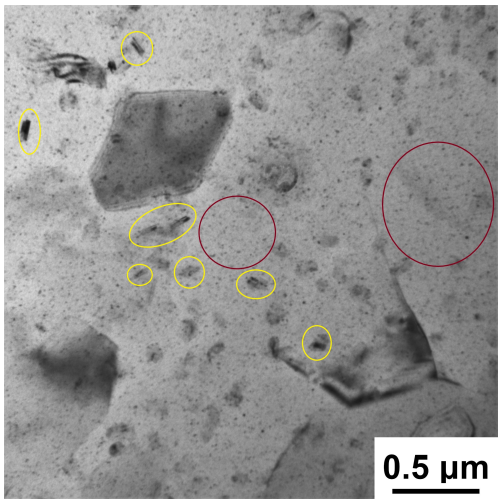

(e) 550 °C

Figure 4.20: In-situ TEM annealing of the specimen after ECAP at temperatures above 350 °C. Red circles mark $Al_3(Sc,Zr)$ precipitates, black ones Al_6Mn phase and yellow circles mark cubic $\alpha - Al_{12}Mn_3Si$.

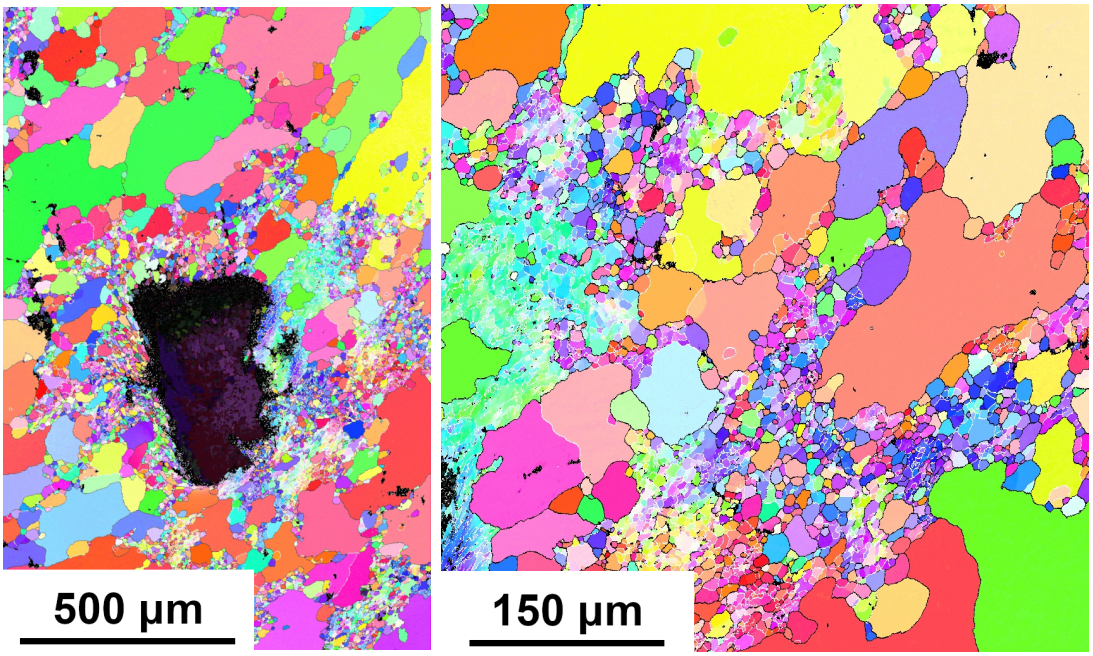

(a) Area near the edge of the hole in the TEM specimen.

(b) Detail of the hole edge vicinity with preserved deformed structure.

Figure 4.21: EBSD inverse pole figures of sample after ECAP annealed in-situ in TEM up to 550 °C.

4.4.4 Bulk annealing up to 550 °C

Due to the thin foil effect on the microstructure evolution during the in-situ annealing a TEM sample was prepared from a billet processed by ECAP, which was annealed in the air furnace in the same step-by-step isochronal heating scheme as the one for microhardnes measurement and EBSD analysis. The microstructure is displayed in the Figure 4.22. The formation of Al_3(Sc,Zr) phase in the matrix above 450 °C was confirmed. However, the average size of the particles coarsened during annealing in the air furnace was about (21 ± 11) nm which means a diameter approximately twice as big in the comparis with those formed during in-situ in TEM annealing – for more details see Figure 4.23c.

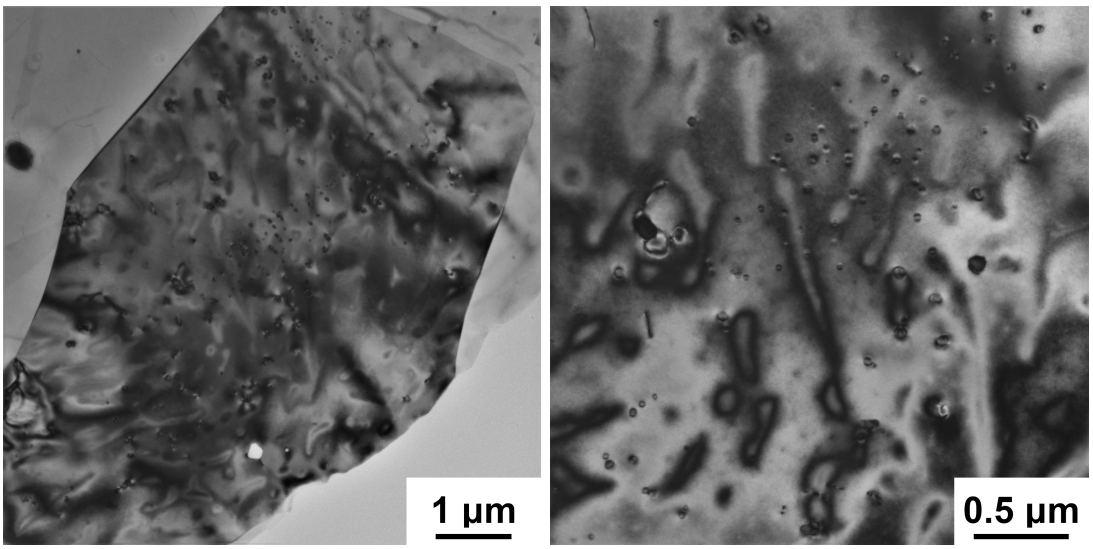

(a) The microstructure of ECAP processed material annealed up to 550 °C.

(b) Bright field image of coarsened Al_3(Sc,Zr) precipitates.

Figure 4.22: The TEM micrographs of the ECAP processed sample annealed isochronally up to 550 °C in an air furnace.

4.4.5 Precipitation of the Al_3(Sc,Zr) phase

Evaluation of the particles size was carried out by ImageJ software, where an automated measurement procedure is available. Results are displayed in histograms in the Figure 4.23.

Dispersion of the Al_3(Sc,Zr) particles was obtained from the projected image of a thin foil. Basically there are two factors – the effect of particles which are cut by the foil surface and the effect of particle overlap on the projected image, which should be considered when the particle size is evaluated [60].

The effect of the cut of the precipitate by the foil surface resulting in an underestimating of its size was neglected due to the small particle size compared to the specimen thickness that is about 50 – 100 nm. The problem of an overestimating of the particles size caused by their overlaps was solved by a selection of a suitable area for the analysis.

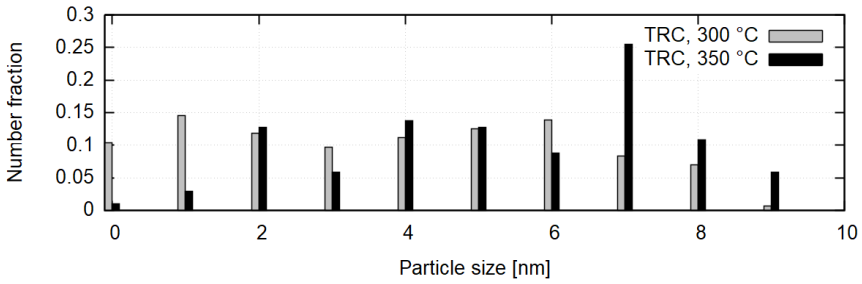

(a) TRC sample annealed in the air furnace isothermally at 300 °C / 8 h and at 350 °C / 8 h.

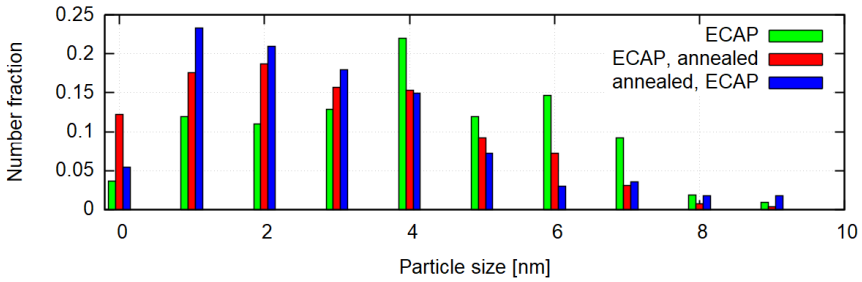

(b) ECAP samples (with and without 300 °C / 8 h pre-annealing) isochronally annealed in the air furnace up to 350 °C.

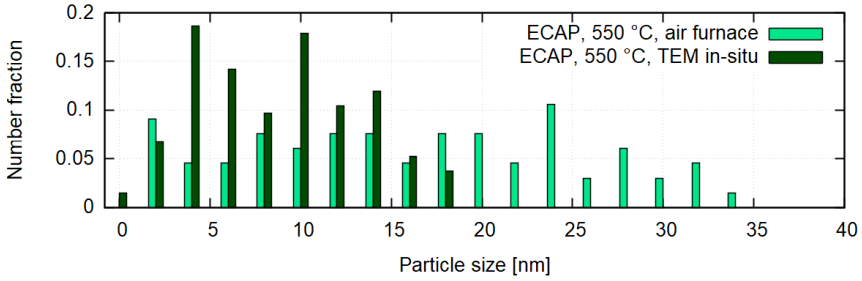

(c) ECAP sample isochronally annealed up to 550 °C in situ in TEM with step 50 °C / 10 min and sample annealed in the air furnace with step 50 °C / 50 min.

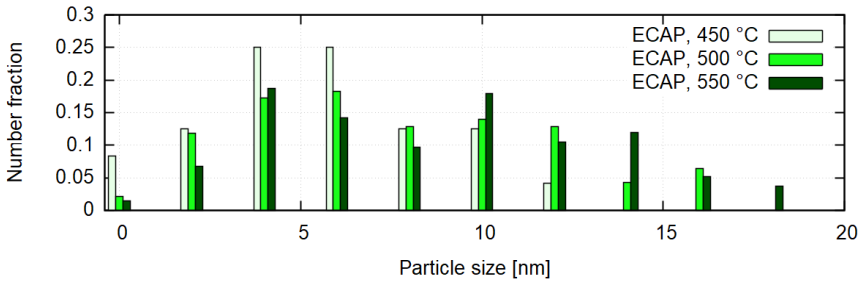

(d) ECAP sample isochronally annealed in-situ in TEM with step 50 °C / 10 min.

Figure 4.23: Histograms of the $Al_3(Sc,Zr)$ particles sizes throughout ECAP processing and annealing experiments.

5. Discussion

The initial microstructure of the as-cast material exhibits features typical for TRC aluminum and magnesium alloys prepared in a mode with a low roll separating force [26]. The central part of the strip contains slightly elongated grains of a size of 50 μm (Figure 4.4), while the ones near the strip surface are noticeably coarser (200 μm) (Figure 1.2). No evidence of the presence of strengthening Al_3(Sc,Zr) particles and a very low dislocation density explain the low initial value of microhardness (Figure 4.11a).

A formation of a fine dispersion of coherent Al_3(Sc,Zr) precipitates (Figure 4.14a) leads to improved mechanical properties due to the precipitation strengthening. The loss of coherency between these hardening precipitates and the Al matrix or particles coarsening (Figure 4.22b) leads to the decrease of the strength.

Annealing at 300 °C / 8 h was chosen as the best option of heat treatment [26]. It induced precipitation of a very fine and uniform distribution of the metastable Al_3(Sc,Zr) phase and fragmentation of the original grains into subgrains (Figure 4.14). As a result, the microhardness increased by about 20 HV compared to the as-cast material (Figure 4.1).

Further enhancement of mechanical properties can be achieved by severe plastic deformation producing considerable grain refinement and strengthening of the material by grain boundaries. Application of the deformation by equal channel angular pressing on the studied twin-roll cast material causes fragmentation of the original grains to micrometric range (Figure 4.5). However, the resulting grain structure is not uniform, the micrometric grains with high angle grain boundaries are often surrounded by elongated subgrains. This is in accordance with observations of Tanski and Sitdikov [61,62] who reported bimodal structure with shear bands in different Al-Mg alloys after various number of ECAP passes. More details can be found in [63].

However, it should be noted that controlling the precipitation kinetics in SPD metals is a crucial issue because there might be competition between recovery, recrystallization and grain growth on one side and heterogeneous precipitation along dislocations and grain boundaries on the other side [64]. SPD methods generally induce large supersaturation of point defects – higher density of vacancies influences the diffusion processes in the material, both during the deformation and after deformation during annealing treatments, and therefore affects the nucleation and growth of the precipitates. Diffusion processes favor heterogeneous precipitation along dislocations and grain boundaries (as sinks for vacancies), which is not desired (Figure 4.18). Moreover, a possible competition can occur between precipitation and recovery of the as-deformed material during the heat treatment. Thus, combination of SPD and precipitation heat treatment were analyzed, especially, their influence on the precipitate morphology and evolution was studied.

The precipitation annealing, applied either before or after ECAP, has no significant influence on the grain microstructure of the deformed material (Figure 4.12 and 4.5). However, it slightly modifies the microhardness of the material (Figure 4.1). Annealing after ECAP at 300 °C for 8 hours causes a slight decrease of the microhardness, which might be connected with a partial recovery

of the dislocation substructure. Also, more pronounced microhardness decrease due to the annealing is most probably compensated by the precipitation of the Al_3(Sc,Zr) phase, and also the strengthening effect of grain boundaries is preserved. However, precipitation of the Al_3(Sc,Zr) phase in the deformed matrix is generally less homogeneous due to a high density of lattice defects induced by ECAP. Indeed, the precipitates form preferentially on the grain boundaries, as confirmed by TEM (Figure 4.17).

Microhardness of the material annealed before ECAP processing is slightly lower than the material which was subjected only to ECAP. This is in accordance with works on a different type of aluminium alloys [65], which showed that annealing before ECAP led to a lower dislocation density after ECAP and finally a lower microhardness. Nevertheless, it is necessary to mention that these differences in microhardness are subtle within the experimental scatter (Figure 4.1b).

Both precipitation annealing 300 °C / 8 h and ECAP applied independently imply increase of microhardness in the material. However, their superposition did not result in a further increase of microhardness, but surprisingly in a slight softening of the material.

In the material pre-annealed 300 °C / 8 h after ECAP, the microhardness remains almost constant during isochronal annealing up to 300 °C (Figure 4.1b) and the repeated application of heat treatment has no significant influence on the material. Slight increase of the microhardness in initial stages of annealing may be attributed to the mechanism described by Huang et al. [66] in a heavily deformed aluminum and observed also in other aluminum alloys [57]. The decrease of the dislocation density during pre-annealing can in such materials result in an increase of the strength during subsequent deformation. As the initial dislocation density is low, new dislocation sources should be activated to enable deformation and, thus, the strength of the material is higher. The distribution of Al_3(Sc,Zr) precipitates after isochronal annealing up to 350 °C (Figure 4.18) exhibits coarser precipitates on grain boundaries (Figure 4.17 and 4.18). They form during the pre-annealing and coarsen during isochronal annealing.The finer particles in the grain interior forms during isochronal annealing.

On the other hand, in the material pre-annealed before ECAP the microhardness slightly increases at temperatures above 200 °C reaching the peak value at 300 °C. It has been reported for several materials [67–69] that severe plastic deformation may lead to a partial dissolution of metastable strengthening particles. As some of the Al_3(Sc,Zr) precipitates probably dissolved during the ECAP processing, their reprecipitation at temperatures close to 300 °C could lead to a further strengthening of the material and increase of the microhardness, masking an eventual softening caused by a recovery of the dislocation substructure (Figure 4.1b). TEM micrographs of the microstructure of this material after isochronal annealing up to 350 °C (Figure 4.18) revealed two generations of Al_3(Sc,Zr) particles – smaller particles that precipitated during isochronal annealing and larger ones that precipitated during pre-annealing, resisted the ECAP deformation and thereafter could coarsen during isochronal annealing. The smaller size of the second generation of particles is in accordance with lower supersaturation of the solid solution. Furthermore, precipitation of both generations of the precipitates seems to be more homogeneous and the shape of the particles is generally more

round than in other deformated materials.

The material processed only by ECAP exhibits the most pronounced changes of the microhardness below 300 °C (Figure 4.1b). Firstly, the microhardness drops to a local minimum at 150 °C. Recovery of the residual dislocation substructure is supposed to occur in this temperature range. On the contrary, microhardness increase is observed at higher annealing temperatures up to 300 °C. This pronounced hardening is attributed to the precipitation of coherent Al_3(Sc,Zr) particles, which has stronger influence on the microhardness than the recovery of the dislocation substructure. Similar behaviour was observed by Vlach et al. [25] in a conventional Al-Sc-Zr alloy after cold rolling. The size and the shape of the precipitates after isochronal annealing up to 350 °C are very unhomogeneous. Dislocation tangles, grain and subgrain boundaries act as short-circuit diffusional paths for Sc atoms. Consequently, ECAP before isothermal annealing can result in heterogeneous nucleation and growth of Al_3(Sc,Zr), because no precipitation nuclei from pre-annealing have been present in this material. All the available Sc and Zr atoms are drained from the matrix and form new precipitates, thus their size is larger than the one observed in the pre-annealed material, where the remaining Sc and Zr atoms from the matrix were consumed by both, the precipitation of new particles and a coarsening of those formed during pre-annealing.

According to [70, 71] Al_3(Sc,Zr) particles precipitated in deformed material could obtain lobed-cuboid or platelet-like rather than spherical morphology, which is in a good correspondence with our observations (Figure 4.18).

Generally, the size of Al_3(Sc,Zr) particles in all ECAP processed materials is smaller than in the undeformed one. Due to the substructure induced by ECAP the preferential sites for nucleation are more numerous, therefore more particles may have nucleated, leading to their overall smaller size.

Further isochronal annealing from 350 °C up to 600 °C brings no general difference between the materials. The microhardness gradually decreases due to the full recovery, recrystallization and the grain growth, reaching the value of around 70 HV observed in non-deformed materials and 65 HV in all ECAP-processed materials (Figure 4.1). Due to a higher stored energy in deformed materials, the recrystallization proceeds to a higher extent, making the final microhardness lower than the one in the non-deformed materials. The Al_3(Sc,Zr) particles coarsen at these temperatures significantly and loose their coherency and their strengthening and boundary pinning effect.

The grain distribution at 550 °C (Figure 4.6 and 4.7) and 600 °C (Figure 4.8 and 4.9) reveals extensive recrystallization between these two temperatures in all deformed samples and full replacement of subgrains by new grains with the size ranging from 10 to 200 μm in all materials. Noticeable bimodal structure with very large grains appears in the ECAP material without pre-annealing caused by a less uniform distribution of Al_3(Sc,Zr) particles formed only during isochronal annealing. Their pinning effect is thus limited, resulting in a higher grain boundary mobility and grain coarsening. The grain structure of remaining two ECAP-ed and pre-annealed samples is also bimodal, however, the final grain size is smaller.

While a full recrystallization was observed in deformed materials after annealing up to 600 °C, undeformed materials contain only partially recrystallized grains located preferentially on high angle grain boundaries of original grains as

a result of a lower stored energy in the grains causing lower driving force for recrystallization. The partially recrystallized grain structure is also consistent with higher values of measured microhardness.

Strengthening mechanisms

In order to evaluate contributions of particular strengthening mechanisms to a final value of the yield strength an estimation based on measured features of the microstructure was done. List of used equations and symbols are given in Table 5.1 and 5.2. Sum of these increments and an intrinsic resistance of the Al lattice to the dislocation motion $\sigma_0 = 60$ MPa [71] gives a total value of yield strength of the material. Even though the estimation suffers from a large experimental errorcaused by the uncertainty of the determination of the thickness of the TEM foil, the estimated values (Table 5.3) exhibit a very good accordance with the measured ones. This consistency of estimated and measured results further supports explanations of observed effect given in the previous paragraph.

Table 5.1: List of the equations for the yield strength increments calculations.

Boundary strengthening	$\Delta\sigma_{\mathrm{HP}} = kD^{-1/2}$
Solid-solution strengthening	$\Delta\sigma_{\mathrm{y}} = \dfrac{3.1\omega G c^{1/2}}{700}$
Precipitate strengthening	
order strengthening	$\Delta\sigma_{\mathrm{ord}} = 0.81M\dfrac{\gamma_{\mathrm{APB}}}{2b}\left(\dfrac{3\pi\phi}{8}\right)^{\frac{1}{2}}$
coherency strengthening	$\Delta\sigma_{\mathrm{coh}} = M\alpha_e(G\theta)^{\frac{3}{2}}\left(\dfrac{R\phi}{0.5Gb}\right)^{\frac{1}{2}}$
modulus mismatch strengthening	$\Delta\sigma_{\mathrm{mod}} = M\alpha_m(\Delta G)^{\frac{3}{2}}\left(\dfrac{2\phi}{G}\right)^{\frac{1}{2}}\left(\dfrac{R}{b}\right)^{\frac{3m}{2}-1}$
Orowan dislocation looping	$\Delta\sigma_{\mathrm{Or}} = M\dfrac{0.4}{\pi}\dfrac{Gb}{\sqrt{1-\nu}}\dfrac{\ln\left(\frac{\sqrt{2/3}R}{b}\right)}{\lambda}$ $\lambda = \left[\left(\dfrac{3\pi}{4\theta}\right)^{\frac{1}{2}} - 1.64\right]R$
Strengthening by dislocations	$\Delta\sigma_{\mathrm{d}} = M\alpha_d Gb\rho^{\frac{1}{2}}$

Table 5.2: List of used symbols of measured material properties and the values of the material constants adopted from the literature

Boundary strengthening			
k	0.17	$\mathrm{MNm}^{3/2}$	material constant for Al-Mg-Li [71]
D			grain size
Solid-solition strengthening			
ω	0.4	-	experimental constant [71]
G	25.4	GPa	shear modulus of Al [71, 72]
c			concentration of Mg in at.%
Precipitate strengthening			
M	3.06	-	mean matrix orientation factor [71]
γ_{APB}	0.5	Jm^{-2}	Al_3Sc antiphase boundary energy [73, 74]
b	0.29	nm	Burgers vector of Al [71]
ϕ			volume fraction of the Al_3(Sc,Zr) phase
α_e	2.6	-	material constant [71]
θ	0.0083	-	constrained lattice parameter mismatch [71]
R			Al_3(Sc,Zr) precipitate radius
α_m	2.6	-	material constant [71]
ΔG	42.5	GPa	shear modulus mismatch: Al and Al_3Sc [75]
m	0.85	-	material constant [71]
ν	0.34	-	Poisson ratio for Al [76]
λ			Al_3(Sc,Zr) inter-precipitate distance
Dislocation strengthening			
α_d	0.11	-	material constant [71, 77]
ρ			dislocation density

Table 5.3: Measured values of the mean grain size, Mg content, dislocation density; volume fraction, radius and inter-precipitate distance of the $Al_3(Sc,Zr)$ phase; predicted and experimental value of the yield strength

	TRC	TRC, annealed	ECAP	TRC 350 °C*	ECAP 350 °C	ECAP, annealed 350 °C	Annealed, ECAP 350 °C	ECAP 550 °C	TRC 600 °C	TRC, annealed 600 °C	ECAP 600 °C	ECAP, annealed 600 °C	Annealed, ECAP 600 °C
D [μm]	39	54	1.7	54	1.7	1.6	1.8	7	36	19	75	48	51
c [at.%]	3.6	3.6	3.6	3.6	3.6	3.6	3.6	3.6	3.6	3.6	3.6	3.6	3.6
ρ [10^{13} m^{-2}]	11.27	7.47	8.09	5.37	3.82	3.02	1.75	0.45	0.10	0.10	0.10	0.10	0.10
θ [%]	0	0.19	0	0.15	0.27	0.10	0.16	0.14	0.13	0.13	0.13	0.13	0.13
R [nm]	0	2.2	0	3.0	2.3	1.7	1.7	10.3	12.4	12.4	12.4	12.4	12.4
λ [nm]	0	75	0	113	64	80	63	404	502	502	502	502	502
$\Delta\sigma_{HP}$ [MPa]	27	23	130	23	130	133	128	66	28	39	20	25	24
$\Delta\sigma_y$ [MPa]	85	85	85	85	85	85	85	85	85	85	85	85	85
$\Delta\sigma_d$ [MPa]	25	21	22	18	15	13	10	5	2	2	2	2	2
$\Delta\sigma_{ord}$ [MPa]	0	102	0	91	123	74	93	89	86	86	86	86	86
$\Delta\sigma_{coh}$ [MPa]	0	26	0	27	32	17	21	49	52	52	52	52	52
$\Delta\sigma_{mod}$ [MPa]	0	99	0	96	121	67	84	132	135	135	135	135	135
$\Delta\sigma_{Or}$ [MPa]	0	107	0	82	129	86	109	37	31	31	31	31	31
$\Delta\sigma_{prec}$ [MPa][a]	0	102	0	82	123	74	93	37	31	31	31	31	31
Total predicted σ [MPa][b]	198	291	297	268	413	365	376	253	207	218	198	203	203
Experimental σ [MPa][c]	256	301	362	323	341	347	336	219	228	229	207	203	208

[a] $\Delta\sigma_{prec} = \min\{\Delta\sigma_{ord}, \Delta\sigma_{coh} + \Delta\sigma_{mod}, \Delta\sigma_{Or}\}$
[b] Sum of four contributions $\Delta\sigma_{HP}$, $\Delta\sigma_y$, $\Delta\sigma_d$, $\Delta\sigma_{prec}$.
[c] Calculated as 3.2619 × HV.

6. Conclusions

Al-Mg-Sc-Zr based alloy was subjected to a precipitation annealing and a severe plastic deformation by ECAP. The influence of these procedures on material strengthening and microstructure and their respective relations were investigated.

The initial TRC strip was pre-annealed and deformed in various orders, therefore five different materials: TRC, TRC + annealed, TRC + ECAP, TRC + ECAP + annealed, TRC + annealed + ECAP, were compared. All these materials were subjected to an isochronal annealing and the evolution of their microstructure and microhardness were evaluated. The results could be summarized in the following items:

- A dispersion of fine particles of the metastable $Al_3(Sc,Zr)$ phase forms during pre-annealing at 300 °C / 8 h in the TRC material. The formation of these particles results in a significant increase of microhardness.
- Severe plastic deformation by ECAP has even stronger influence on the microhardness of the TRC strip.
- Pre-annealing 300 °C / 8 h of specimens before or after ECAP does not provide an expected further increase of microhardness due to a heterogeneous formation of strengthening particles and partial recovery of the deformed substructure or partial deformation induced precipitates dissolution (ECAP after pre-annealing)
- Peak hardening during isochronal annealing was achieved in all specimens at 350 °C independently on a previous thermo-mechanical treatment.
- A degradation of the material properties occurs above 350 °C caused by a recrystallization of the material and coarsening of strengthening particles of the $Al_3(Sc,Zr)$ phase.
- The final microhardness after isochronal annealing up to 600 °C measured in all specimen after ECAP is lower than the value of microhardness in the as-cast material. The main reason is a lower amount of deformation energy stored during ECAP and subsequent full recrystallization and grain coarsening, while only a partial recovery and recrystallization were observed in the TRC material.
- Measured values of microhardness are in a good accordance with a sum of contributions to the material strengthening predicted by theoretical models.

Bibliography

[1] UC RUSAL. Aluminum in power-engineering. https://www.aluminiumleader.com/application/electrical_engineering. Accessed: 2019-04-22.

[2] Encyclopædia Britannica. Aluminum, chemical element. https://www.britannica.com/science/aluminum. Accessed: 2019-04-22.

[3] John E. Hatch. *Aluminum: Properties and Physical Metallurgy*. Aluminum Association Inc. and ASM International, 1984.

[4] Xuesong Zhanga, Yongjun Chen, and Junling Hu. Recent advances in the development of aerospace materials. *Progress in Aerospace Sciences*, 97:22–34, 2018.

[5] Hui Li, Zhaohui Yan, and Lingyong Cao. Bake hardening behavior and precipitation kinetic of a novel Al-Mg-Si-Cu aluminum alloy for lightweight automotive body. *Materials Science and Engineering: A*, 728:88–94, 2018.

[6] Vadim S. Zolotorevsky, Nikolai A. Belov, and Michael V. Glazoff. *Casting Aluminum Alloys*. Elsevier Science, 2007.

[7] Jess A. Lyndon, Rajeev K. Gupta, Mark A. Gibson, and Nick Birbilis. Electrochemical behaviour of the β-phase intermetallic (Mg2Al3) as a function of pH as relevant to corrosion of aluminium–magnesium alloys. *Corrosion Science*, 70:290–293, 2013.

[8] John E. Hatch. *Aluminum: Properties and Physical Metallurgy*. Aluminum Association Inc. and ASM International, 1984.

[9] David Darling 2016. Terrestrial abundance of elements. http://www.daviddarling.info/encyclopedia/E/elterr.html. Accessed: 2019-04-22.

[10] Israel Science and Technology Directory. Chemistry : List of Periodic Table Elements. https://www.science.co.il/elements/?s=Name. Accessed: 2019-04-22.

[11] Michael E. Donoghue, Neale Frisch, and David Olney. Bauxite Mining and Alumina Refining: Process Description and Occupational Health Risks. *Journal of Occupational and Environmental Medicine*, 56:S12–S17, 2014.

[12] USGS. Bauxite and Alumina, Statistics and Information. https://minerals.usgs.gov/minerals/pubs/commodity/bauxite/. Accessed: 2019-04-22.

[13] Wheeler P. Davey. Precision Measurements of the Lattice Constants of Twelve Common Metals. *Physical Revue*, 25:753–761, 1925.

[14] John E. Hatch. *Aluminum: Properties and Physical Metallurgy*. Aluminum Association Inc. and ASM International, 1984.

[15] M. Peach and James S. Koehler. The Forces Exerted on Dislocations and the Stress Fields Produced by Them. *Physical Revue*, 80:436–439, 1950.

[16] Ulrich Fred Kocks. Kinetics of solution hardening. *Metallurgical Transactions A*, 16:2109–2129, 1985.

[17] Reiner Labusch. Statistische theorien der mischkristallhärtung. *Acta Metallurgica*, 20:917–927, 1972.

[18] Pavel Lukáč (I. Mechanismy zpevnění a odpevnění). *Zpevnění materiálu a rekrystalizace (Učební texty z cyklu přednášek Materiálové inženýrství na VŠB)*. Vysoká škola Báňská v Ostravě - Porubě, 1992.

[19] Michael F. Ashby. Results and consequences of a recalculation of the frank-read and the orowan stress. *Acta Metallurgica*, 14:679–681, 1966.

[20] M.C. Carroll, Pelagia Gouma, M.J. Mills, Glenn S. Daehn, and B.R. Dunbar. Effects of Zn additions on the grain boundary precipitation and corrosion of Al-5083. *Scripta Materialia*, 42, 2000.

[21] K. Sharp, T. Mills, Graham Clark, and S. Russo. Recent advances in modelling exfoliation corrosion. Sydney, 2000.

[22] R. Vissers, Marijn van Huis, J. Jansen, Henny Zandbergen, Calin Daniel Marioara, and Sigmund Jarle Andersen. The crystal structure of the β-phase in Al–Mg–Si alloys. *Acta Materialia*, 55:3815–3823, 2007.

[23] John E. Hatch. *Aluminum: Properties and Physical Metallurgy*. Aluminum Association Inc. and ASM International, 1984.

[24] Vadim S. Zolotorevsky, Nikolai A. Belov, and Michael V. Glazoff. *Casting Aluminum Alloys*. Elsevier Science, 2007.

[25] Martin Vlach, Ivana Stulíková, Bohumil Smola, Naďa Žaludová, and Jaroslava Černá. Phase transformations in isochronally annealed mould-cast and cold-rolled Al–Sc–Zr-based alloy. *Journal of Alloys and Compounds*, 492:143–148, 2010.

[26] Miroslav Cieslar, Jan Bajer, Mariia Zimina, Michaela Šlapáková, and Olexandr Grydin. Properties and microstructure of twin-roll cast Al-Mg alloy containing Sc and Zr. *IOP Conf. Series: Materials Science and Engineering*, 2017.

[27] Miroslav Cieslar, Jan Bajer, Michaela Šlapáková, Barbora Křivská, Mariia Zimina, Mykhailo Stolbchenko, and Olexandr Grydin. The influence of annealing on microstructure and microhardness of twin-roll cast Al-Mg-Sc-Zr alloy. *Acta Physica Polonica A*, 134:145–149, 2018.

[28] Ming Yun, S. Lokyer, and John D. Hunt. Twin roll casting of aluminium alloys. *Materials Science and Engineering: A*, 280:116–123, 2000.

[29] Margarita Slámová, Miroslav Karlik, Florence Robaut, Peter Sláma, and Muriel Véron. Differences in microstructure and texture of Al–Mg sheets produced by twin-roll continuous casting and by direct-chill casting. *Materials Characterization*, 49:231–240, 2003.

[30] Dmitri Kopeliovich. Continuous casting in traveling mold. `http://www.substech.com/dokuwiki/doku.php?id=continuous_casting_in_traveling_mold#twin-roll_caster`. Accessed: 2019-04-22.

[31] Niels Hansen. Hall-Petch and boundary strengthening. *Scripta Materialia*, 51:801–806, 2004.

[32] Michaela Šlapáková, Mariia Zimina, Stefan Zaunschirm, Johann Kastner, Jan Bajer, and Miroslav Cieslar. 3D analysis of macrosegregation in twin-roll cast AA3003 alloy. *Materials Characterization*, 118:44–49, 2016.

[33] Michaela Šlapáková, Barbora Křivská, Olexander Grydin, and Miroslav Cieslar. The influence of casting methods on microstructure of Al-Mg-Sc-Zr alloy. *Manufactoring Technology*, 18:130–134, 2018.

[34] A. Azushima, R. Kopp, A. Korhonen, D.Y. Yang, F. Micari, G.D. Lahoti, P. Groche, J. Yanagimoto, N. Tsuji, A. Rosochowski, and A. Yanagida. Severe plastic deformation (SPD) processes for metals. *CIRP Annals*, 57:716–735, 2008.

[35] Peter Fajfar, Alenka Salej Lah, Jakob Kraner, and Goran Kugler. Asymmetric rolling process. *Materials and Geoenvironment*, 64, 2017.

[36] Mahnoosh Shaarbaf and Mohammad Reza Toroghinejad. Nano-grained copper strip produced by accumulative roll bonding process. *Materials Science and Engineering: A*, 473:28–33, 2008.

[37] Fatemeh Zahra Hassani and Mostafa Ketabchi. Nano grained AZ31 alloy achieved by equal channel angular rolling process. *Materials Science and Engineering A*, 528:6426–6431, 2011.

[38] Jae-Chul Lee, Hyun-Kwang Seok, and Jin-Yoo Suh. Microstructural evolutions of the Al strip prepared by cold rolling and continuous equal channel angular pressing. *Acta Materialia*, 50:4005–4019, 2002.

[39] Amit Kumar Gupta, Tejveer Simha Maddukuri, and Swadesh Kumar Singh. Constrained groove pressing for sheet metal processing. *Progress in Materials Science*, 84:403 – 462, 2016.

[40] Dong Hyuk Shin, Jong-Jin Park, Yong-Seog Kim, and Kyung-Tae Park. Constrained groove pressing and its application to grain refinement of aluminum. *Materials Science and Engineering: A*, 328:98–103, 2002.

[41] Jan Bajer, Miroslav Cieslar, Michaela Šlapáková, Mariia Zimina, Z. Nový, and A. Materna. Grain Structure and Microhardness Development of Twin-Roll Cast Aluminum Strips after Constrained Groove Pressing. *Acta Physica Polonica*, 134:909–912, 2018.

[42] Olexandr Grydin, Mykhailo Stolbchenko, Florian Nürnberger, and Mirko Schaper. Influence of the Twin-Roll Casting Parameters on the Microsegregation in Thin Strips of the Aluminium Alloy EN AW-6082. *TMS Light Metals*, pages 411–414, 2014.

[43] Margarita Slámová, Vladivoj Očenášek, and George Frederic Vander-Voort. Polarized light microscopy: utilization in the investigation of the recrystallization of aluminum alloys. *Materials Characterization*, 52:165–177, 2004.

[44] VAC AERO. Color Metallography. `https://vacaero.com/information-resources/metallography-with-george-vander-voort/991-color-metallography.html`. Accessed: 2019-04-22.

[45] Leica Microsystems. Metallography, Light optical microscopy. `https://www.leica-microsystems.com/science-lab/metallography-an-introduction/`. Accessed: 2019-04-22.

[46] Metallographic Imaging Modes. `https://www.metallography.com/technotes/imaging/imaging2.htm`. Accessed: 2019-04-22.

[47] Claude Dalton. Metallographic Etching of Aluminum. `https://docplayer.net/38808493-Metallographic-etching-of-aluminum-and-its-alloys.html`. Accessed: 2019-04-22.

[48] Electron Backscatter Diffraction. `https://www.tescan.com/en-us/technology/detectors/electron-backscatter-diffraction`. Accessed: 2019-04-22.

[49] Oxford Instruments Plc. Kikuchi Pattern Formation. `http://www.ebsd.com/ebsd-explained/pattern-formation`. Accessed: 2019-04-22.

[50] EDAX Company. OIM Analysis. `https://www.edax.com/products/ebsd/oim-analysis`. Accessed: 2019-04-22.

[51] David B. Williams and C. Barry Carter. *Transmission Electron Microscopy*. Springer, 2009.

[52] Miroslav Karlík. *Úvod do transmisní elektronové mikroskopie*. ČVUT, 2011.

[53] Barbora Křivská, Michaela Šlapáková, Jan Bajer, Miroslav Cieslar, Olexandr Grydin, and Mykhailo Stolbchenko. The Influence of Al-Mg-Sc-Zr Strips Preparation on Microhardness During Annealing at Elevated Teperatures. In *Metal 2018 Conference Proceedings*, pages 1593–1598, Brno, 2018.

[54] Laszlo S. Toth, Somjeet Biswas, Chengfan Gu, and Benoit Beausir. Notes on representing grain size distributions obtained by electron backscatter diffraction. *Materials Characterization*, 84:67–71, 2013.

[55] George E. Totten, Murat Tiryakioglu, and Olaf Kessler. *Encyclopedia of Aluminum and Its Alloys*. CRC Press, 2018.

[56] Marco J. Starink, Xiao Guang Qiao, Jiuwen Zhang, and Nong Gao. Predicting grain refinement by cold severe plastic deformation in alloys using volume averaged dislocation generation. *Acta Materialia*, 57:5796–5811, 2009.

[57] Michaela Šlapáková, Mariia Zimina, and Miroslav Cieslar. Effect of preannealing on microstructure evolution ofTRC AA3003 aluminum alloy subjected to ECAP. *Transactions of Nonferrous Metals Society of China*, 26:627–633, 2016.

[58] Martin Vlach, Jakub Čížek, Bohumil Smola, Oksana Melikhova, Marián Vlček, Veronika Kodetová, Hana Kudrnová, and Petr Hruška. Heat treatment and age hardening of Al–Si–Mg–Mn commercial alloy with addition of Sc and Zr. *Materials Characterization*, 129:1–8, 2017.

[59] Michaela Poková, Mariia Zimina, and Miroslav Cieslar. The Influence of Equal Channel Angular Pressing on Microstructure Evolution during Insitu Heating in Transmission Electron Microscope. *International Journal of Materials Research*, 106:676–681, 2015.

[60] P. B. Hirsch, A. Howie, R. B. Nicholson, D. W. Pashley, and M. J. Whelan. *Electron microscopy of thin crystal*. PLENUM PRESS, New York, 1967.

[61] T. Tański, P. Snopiński, K. Prusik, and M. Sroka. The effects of room temperature ECAP and subsequent aging on the structure and properties of the Al-3Mg aluminium alloy. *Materials Characterization*, 133:185–195, 2017.

[62] O. Sitdikov, T. Sakai, E. Avtokratova, R. Kaibyshev, K. Tsuzaki, and Y. Watanabe. Microstructure behavior of Al–Mg–Sc alloy processed by ECAP at elevated temperature. *Acta Materialia*, 56:821–834, 2008.

[63] Michaela Šlapáková, Barbora Křivská, Jan Bajer, Olexandr Grydin, and Miroslav Cieslar. Al-Mg-Sc Alloys processed by Equal-Channel Angular Pressing. In *Metal 2017 Conference Proceedings*, pages 1501–1506, Brno, 2017.

[64] Amélie Fillon, X. Sauvage, Arnaud Pougis, Olivier Bouaziz, David Barbier, Roxane Arruffat, and Laszlo Toth. Influence of severe plastic deformation on the precipitation hardeningof a FeSiTi steel. *Journal of Materials Science*, 47, 2012.

[65] Michaela Šlapáková, Mariia Zimina, and Miroslav Cieslar. Effect of preannealing on microstructure evolution of TRC AA3003 aluminum alloy subjected to ECAP. *Transactions of Nonferrous Metals Society of China*, 26:627–633, 2016.

[66] X. Huang, N. Kamikawa, and N. Hasen. Strengthening mechanism in nanostructured aluminium. *Materials Science and Engineering A*, 483-484:102–104, 2008.

[67] Boris B. Straumal, Askar R. Kilmametov, Yulia Ivanisenko, Andrei A. Mazilkin, Olga A. Kogtenkova, Lilia Kurmanaeva, Anna Korneva, Pawel Zieba, and Brigitte Baretzky. Phase transitions induced by severe plastic

deformation: steady-state and equifinality. *International Journal of Materials Research*, 106:657–664, 2015.

[68] Omid Nejadseyfi, Ali Shokuhfar, Amirreza Dabiri, and Amin Azimi. Combining equal-channel angular pressing and heat treatment to obtain enhanced corrosion resistance in 6061 aluminum alloy. *Journal of Alloys and Compounds*, 648:912–918, 2015.

[69] Zhiyi Liu, Song Bai, Xuanwei Zhou, and Yanxia Gu. On strain-induced dissolution of θ' and θ particles in Al–Cu binary alloy during equal channel angular pressing. *Materials Science and Engineering: A*, 528:2217–2222, 2011.

[70] Yu. Buranova, V. Kulitskiy, M. Peterlechner, A. Mogucheva, R. Kaibyshev, S.V. Divinski, and G. Wilde. Al_3(Sc,Zr)-based precipitates in Al–Mg alloy: Effect of severe deformation. *Acta Materialia*, 124:210–224, 2017.

[71] Nhon Q. Vo, David C. Dunand, and David N. Seidman. Atom probe tomographic study of a friction-stir-processed Al–Mg–Sc alloy. *Acta Materialia*, 60:7078–7089, 2012.

[72] Engineering ToolBox. Modulus of Rigidity . `https://www.engineeringtoolbox.com/modulus-rigidity-d_946.html`. Accessed: 2019-05-16.

[73] C. L. Fu. Electronic, elastic, and fracture properties of trialuminide alloys: Al3Sc and Al3Ti. *Journal of Materials Research*, 5:971–979, 1990.

[74] K. Fukunaga, M. Kolbe, K. Yamada, and Y. Miura. Temperature dependence of dislocation dissociation mode in L12 trialuminides. *Materials Science and Engineering: A*, 234-236:594 – 597, 1997.

[75] R.W. Hyland and R.C. Stiffler. Determination of the elastic constants of polycrystalline Al3Sc. *Scripta Metallurgica et Materialia*, 25:473 – 477, 1991.

[76] Engineering ToolBox. Poisson ratio. `https://www.engineeringtoolbox.com/poissons-ratio-d_1224.html`. Accessed: 2019-05-16.

[77] Jian Lan, Xuejun Shen, Juan Liu, and Lin Hua. Strengthening mechanisms of 2A14 aluminum alloy with cold deformation prior to artificial aging. *Materials Science and Engineering: A*, 745:517 – 535, 2019.